Growth of accreting intermediate mass black hole seeds

G. Ter-Kazarian*

Byurakan Astrophysical Observatory, Byurakan, Aragatsotn Province, Armenia

Abstract

This communication aims to review the mass assembly history of seed black holes to the present time of accreting intermediate mass black hole (IMBH)-candidates. Given the masses and redshifts at present time of 137 IMBH-candidates collected from the literature, we have undertaken a large series of numerical simulations to achieve this goal. The crux is that, we utilize the *microscopic theory of black hole* (MTBH), which explores the most important novel aspects expected from considerable change of properties of space-time continuum at spontaneous breaking of gravitation gauge symmetry far above nuclear density. As a corollary, this theory has smeared out the central singularities of BHs, and makes room for their growth and merging behavior. We compute among the others the masses, the growth-time scales, T_{BH}, and the redshifts of seed BHs. In particular, for the present masses $\log(M/[\mathrm{M_\odot}]) = 2.20$ to 5.99 of IMBH-candidates, the computed seed masses are ranging from $\log(M^{seed}/[\mathrm{M_\odot}]) = -0.50$ to 3.29, with corresponding growth-time scales T_{BH} ranging from $\log(T_{BH}/[\mathrm{yr}]) = 8.82$ to 10.09. We derived scaling mass-luminosity relation, by means of which we compute the luminosities of IMBH-candidates ranging from $\log(L/[\mathrm{erg\,s^{-1}}]) = 39.13$ to 41.653.

Keywords: *black hole physics–intermediate mass black holes–galaxies: dwarf–globular clusters–ULXs and HLXs*

1. Introduction

One of the achievements of present observational astrophysics is the development of a quite detailed study of the physical properties of growth and merging phenomena of astrophysical black holes, even at its earliest stages. Although proving the existence of seed BHs in the early Universe is not yet feasible with the current instrumentation, remained below the observational capabilities, the detection and study of those seed BHs that did not grow into supermassive BHs (SMBHs), can be found as IMBHs in the nearby Universe. In past decades, the debate about population of IMBHs was less fettered by observational evidence, but it gathers support from a breakthrough made in recent observational efforts (e.g. Baldassare & Reines, 2015, Baldassare & et al., 2016, Barth et al., 2004, Baumgardt, 2017, Chen & Shen, 2018, Feldmeier et al., 2009, Ferrarese & Merritt, 2000, Fragione et al., 2018, Gallerani et al., 2017, Gebhardt & et al., 2000, Gerssen et al., 2002, Graham & Scott, 2013, Harrison, 2018, Ho & Kim, 2016, Inayoshi & Visbal, 2019, Johnson & Haardt, 2016, Kaaret & Feng, 2017, Katz et al., 2015, Kiziltan et al., 2017, Koliopanos, 2017, Latif & Ferrara, 2016, Latif & Schleicher, 2018, Lützgendorf et al., 2012, 2013, Nguyen et al., 2017, Noyola & Gebhardt, 2010, Perera & Stappers, 2018, Perera et al., 2017, Reines et al., 2013, Sakurai et al., 2017, Soria et al., 2017, Takekawa et al., 2019, Wang et al., 2015, Webb, 2017, Woods et al., 2019, Xiao et al., 2011), and at present it would require a good deal more ingenuity, which is of immense significance for their formation and growth. The multiwavelength methods, used to trace the growth of seed BHs, suggest that a population of IMBHs, very likely, exists. For an up-to-date review of all the observational evidence found so far and the different evolutionary pathways for creation of IMBHs, see (e.g. Inayoshi & Visbal, 2019, Koliopanos, 2018, Mezcua, 2017)). This has strong implications for understanding of key questions how the seeds of massive BHs may have first assembled, and how did they grow into IMBHs. The study of accretion physics of IMBHs is of vital interest for evaluating the role of the BH in the formation of the first galaxies.

However, even thanks to the fruitful interplay between theoretical and computational analysis, and astronomical observations, the scientific situation remains, in fact, more inconsistent to day. A systematic analysis of these properties happens to be surprisingly difficult by conventional theoretical methods. A

---

principle feature that makes general relativity (GR) distinctively different from other field theories is the occurrence of curvature singularities in spacetime. The singularities lead to regions of the Universe that cannot be observed. This causes an observer's inability to access the degrees of freedom that are hidden beyond the horizon which, in turn, leads to thermodynamical behavior of BHs. Notwithstanding, much remarkably efforts have been made in understanding of BH physics, many important issues still remain unresolved and, thus, a situation is unclear, than described so far. The astrophysical significance of the issue, and the importance of considering the gravitational collapse of a matter cloud within the framework of the GR theory, with reasonable physical properties for the matter included, stems from the fact that GR predicts that a star more massive than about five to eight times the mass of the Sun, cannot stabilize to a neutron star final state at the end of its life cycle. Thereby the estimates on the mass limit for a star in order to collapse are indefinitely vary depending on different models for the star's interior and equation of state for matter at very high densities. It must collapse continually under the force of its own gravity on exhausting its internal nuclear fuel, and there are no known forces of nature that would halt such a collapse. General relativity predicts that such a star must then terminate into a spacetime singularity where densities and spacetime curvatures blow up and the physical conditions are extreme. One of the most important open issues in the theory and astrophysical applications of modern day BH and gravitation physics is that of the Roger Penrose's Cosmic Censorship Conjecture (CCC) (Laporte et al., 1969). The CCC assumption that any physically realistic gravitational processes must not lead to the formation of a singularity which is not covered by an horizon, thus hiding it from external observers in the Universe. This of course includes the complete gravitational collapse of a massive star which, if the CCC is true, must terminate generically into a BH final state only. Such a singularity is then crucial and is at the basis of much of the modern theory and astrophysical applications of BHs today. Despite the past four decades of serious efforts, we do not have as yet available any proof or even any mathematically precise formulation of the cosmic censorship hypothesis.

The consideration of dynamical evolution of collapse is a crucial element of the CCC. Many solutions of Einstein field equations are known which present naked singularities (such as, for example, the super-spinning Kerr solutions), nevertheless almost none of these solutions can be obtained as the dynamically evolved final state of some initially regular matter configuration. For this reason, over the last decades a great deal of work has been done to test the CCC in the few dynamically evolving spacetimes we know. These are typically the scenarios that describe gravitational collapse in spherical symmetry, and some non-spherical collapse models have also been considered, for examples of critical collapse with angular momentum. The incredibility of such an inference of CCC has been greatly enhanced by the fuct that in recent years, a wide variety of gravitational collapse models have been discovered where exact analytical calculations (e.g. Giambo et al., 2004, Goswami & Joshi, 2002, Joshi & Malafarina, 2011, 2013, Villas da Rocha & Wang, 2000) and references therein) have meanwhile shown that mass concentrations collapsing under their own weight will no longer form BHs as collapse endstate, rather naked singularities, except for configurations of highest symmetry which are, however, of measure zero among all initial data. By this, even the theoretical existence of BHs is no longer justified. The first examples were restricted to some classes of inhomogeneous dust collapse, and they were extended to the case of collapse in the presence of only tangential pressures, and perfect fluids. The existence of classes of pressure perturbations is shown explicitly, which has the property such that an injection of a small positive (or negative) pressure in the Oppenheimer, Snyder and Datt (OSD) model (Datt, 1938, Oppenheimer & Snyder, 1939), or in a Tolman-Bondi-Lemaitre (TBL) inhomogeneous dust collapse to a BH, leads the collapse to form a naked singularity, rather than a BH (Joshi & Malafarina, 2011, 2013). The classic OSD scenario is the basic paradigm for BH physics today, and the TBL models describe the most general family of dust, i.e. pressureless, collapse solutions. This result is therefore intriguing, because it shows that arbitrarily close to the dust BH model, we have collapse evolutions with non-zero pressures that go to a naked singularity final state, thus proving a certain 'instability' of the OSD BH formation picture against the introduction of small pressure perturbations. In such a case, the super-ultra-dense regions, or the spacetime singularity, that forms at the end of collapse would be visible to faraway observers in the Universe, rather than being hidden in a BH. Thus, rigorous calculations have shown that the expectations of the 1970s have been hasty, that CCC assumption has been premature, because while the CCC states that the OSD collapse final fate is necessarily replicated for any realistic stellar collapse in nature, the result here shows that an arbitrarily small pressure perturbation of the OSD model can change the final outcome of collapse to a naked singularity and therefore the OSD BH may be considered 'unstable' in this sense. Moreover, there is no provision for growth and merging behavior of seed BHs in the framework of phenomenological BH model (PBHM), as peculiar repercussion of GR, because of the nasty inherent appearance of BH *singularities*, and that if the *infinite collapse to the singularity* inside the BH is accepted

as a legitimate feature of Nature. Although it is extremely hard to envisage a consistent theory having such a logical impossibility, this problem stood open for nearly a century as a startling preoccupation of wide community of theoreticians (see Ter-Kazarian (e.g. 2014, 2015b, 2016a,b), Ter-Kazarian & Shidhani (e.g. 2017, 2019) and references therein).

Refining our conviction that a complete, *self - consistent* gravitation theory will smear out singularities at huge energies, and give the solution known deep within the BH, in what follows we advocate with alternative proposal by employing the MTBH, which has explored the most important novel aspects expected from considerable change of properties of space-time continuum at spontaneous breaking of gravitation gauge symmetry far above nuclear density. Explaining in more detail the physical arguments behind the microscopic model of IMBH, therefore, the present article is widely based on the premises of the study of internal structure of IMBHs (Ter-Kazarian & Shidhani, 2019), where we tackled the problems in the theoretical framework of MTBH. In this, we have undertaken a large series of numerical simulations to obtain the integral characteristics of 137 IMBH-candidates. Continuing along this line, in present article we discuss the implications of microscopic model for tracing a mass assembly history of these candidates. These peculiarities deserve careful study. First, because they can be expected to lead to particularly sensitive tests of the theory if they can be subjected to experimental scrutiny. Second, because they furnish valuable theoretical clues about the interpretation and significance of the theory of growth and merging behavior of BHs. Needless to say that we will refrain from providing lengthy details of MTBH. We will not be concerned with the actual details of the MTBH here, but only use it as a backdrop to validate the MTBH with some observational tests. Wherever new results follow from earlier work, we restricted ourself only by a simple reference to earlier papers.

With this perspective in sight, we will proceed according to the following structure. The key objectives of MTBH are briefly outlined in Section 2. In Section 3, we provide a brief discussion of a growth of seed BH driven by an accretion and calculate its mass. In Section 4, we derive an analytical expression for the BH's ' neutrino pre-radiation time' (PRT). We also provide a scaling mass-luminosity relation of IMTB. In Section 5, we calculate the redshift of seed BH. In Section 6, we outline the microscopic model building, research design and methods. The Section 7 deals with the state equation in use, step-by-step away from the domain of lower density up to the domain of higher density. The results of simulation are presented in Section 8. The concluding remarks are given in Section 9. A few more technical details in use are deferred to appendices. In Appendix A, we briefly outline the key points of underlying gravitation theory, discuss a spontaneous breaking of gravitation gauge symmetry and, as a corollary, so-called *inner distortion* (ID) of spacetime continuum. Appendix B deals with the field equations of non-spinning SPC in ID regime, and provide the state equation of baryonic proto-matter. In Appendix C, we explain some technical details of spinning SPC.

2. The MTBH, revisited

For a benefit of the reader, as a guiding principle to make the rest of paper understandable, in this section we necessarily recount some of the highlights behind of MTBH, which are in use throughout the paper. We extend preceding developments of the model of a non-rotating SPC (Ter-Kazarian, 2010, 2014, 2015b, 2016a,b, Ter-Kazarian & Shidhani, 2017, and references therein), without going into the subtleties, as applied to the study of BH-growth. There are several important topics not touched upon here, which will eventually benefit from the proposed theory. Although some key theoretical ideas were introduced with a satisfactory substantiation, we have also attempted to maintain a balance between being overly detailed and overly schematic.

The MTBH was extension of PBHM and rather completes it by exploring the most important processes of spontaneous breaking of gravitation gauge symmetry at huge energies. The latter yields a significant change of properties of spacetime continuum: the ID-regime. To clarify the distinction between the PBHM and the MTBH, it should help a few noteworthy points of Fig. 1 which schematically plotted the BH in phenomenological and microscopic frameworks.

A crucial point of the MTBH is that a central singularity cannot occur, which is now replaced by finite though unbelievably extreme conditions held in the equilibrium, so-called, superdense proto-matter core (SPC) inside the EH, subject to certain rules, where the static observers are existed. Consisting of the proto-matter core and the outer layers of ordinary matter, the SPC-configuration is the spherical-symmetric distribution of matter in many-phase stratified states. A layering is a consequence of the onset of different
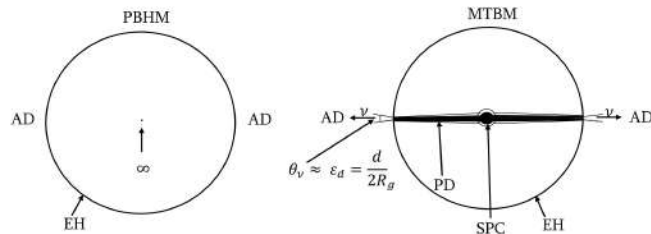
Figure 1. *Left panel*: Phenomenological model of non-spinning BH. The meaningless singularity occurs at the center inside the BH. *Right panel*: Microscopic model of non-spinning BH, with the central stable SPC inside the EH. An infalling matter with the time forms PD around the SPC. In final stage of growth, a PD has reached out the edge of the event horizon. Whereas a metric singularity inevitably disappears and UHE neutrinos may escape from event horizon to outside world through vista - a thin belt area $S = 2\pi R_g d$ - with opening angle θ_ν. Accepted notations: EH=Event Horizon, AD=Accretion Disk, SPC=Superdense Proto-matter Core, PD=Proto-matter Disk.
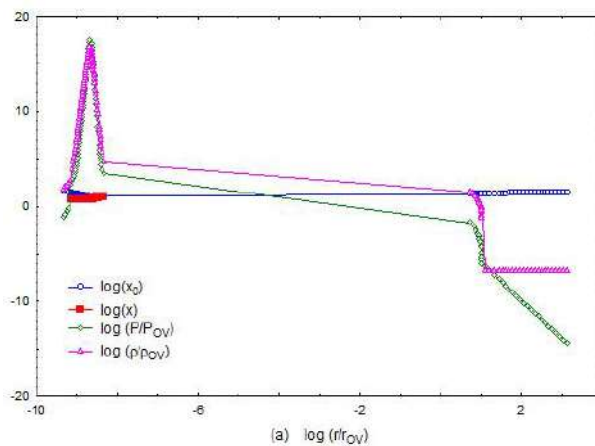

Figure 2. The radial profiles of the pressure, the density, the dimensionless gravitational (x_0)- and ID (x)-potentials of the SPC-configuration of mass $\sim 6.31 \times 10^3 \, M_\odot$.

regimes in equation of state. The simulations confirm in brief the following scenario. The energy density and internal pressure have sharply increased in proto-matter core, with respect to corresponding central values of neutron star, proportional to gravitational forces of compression. This counteracts the collapse and equilibrium holds even for the masses up to $\sim 10^{10} M_\odot$. Encapsulated in a complete set of equations of SPC-configuration, the SPC is a robust structure that has stood the tests of the most rigorous theoretical scrutinies of its stability (Ter-Kazarian et al., 2007). Minimizing the total energy gives the equilibrium configurations. The second derivative of total energy gives stability information. Although a relativity tends to destabilize configurations, however, a numerical integrations of the stability equations of SPC clearly proves the stability of resulting cores. Due to it, the stable equilibrium holds in outward layers too and, thus, an accumulation of matter is allowed now around the SPC. The seed BH might grow up driven by the accretion of outside matter when it was getting most of its mass.

Without loss of generality, the typical features of SPC-configurations are summing up in the Fig. 2 and Fig.3, to guide the eye. The radial profiles of the pressure, the density, the dimensionless gravitational (x_0)- and *inner distortion* (ID) (x)- potentials (see App. A) are plotted in Fig.2, for example, for the given SPC-configuration of the mass $\sim 6.31 \times 10^3 \, M_\odot$ (that of the Sun, $M_\odot$), and the state equation is presented in Fig.3. The special units in use denote $P_{OV} = 6.469 \times 10^{36} \, \mathrm{erg \, cm^{-3}}$, $\rho_{OV} = 7.195 \times 10^{15} \, \mathrm{g \, cm^{-3}}$ and $r_{OV} = 13.68 \, \mathrm{km}$. As it is seen, the MTBH is in good agreement with general relativity up to the limit of neutron stars. Moreover, above nuclear density, the SPC always resides inside the event horizon, therefore it could be observed only in presence of accreting matter. The external physics of accretion onto the SPC in first half of its lifetime is identical to the processes in phenomenological BH models. In other words, there is no observable difference between the gravitational field of SPC and Schwarzschild BH, so that the observable signature of BHs available in literature is of direct relevance for the SPC-configurations too. But MTBH manifests its virtue when one looks for the internal physics, accounting for growth and merging behavior of
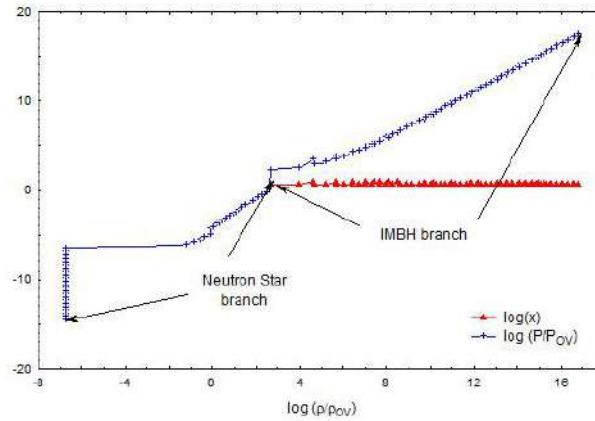
Figure 3. The state equation of the SPC-configuration of mass $\sim 6.31 \times 10^3 \, M_\odot$.
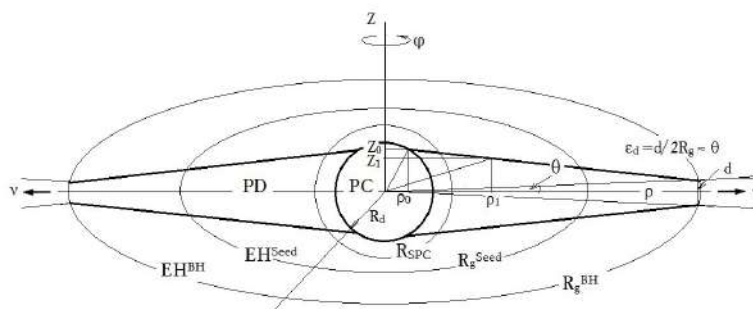

Figure 4. A schematic cross section of the growth of a BH driven by a formation of the proto-matter (PD) disk at accretion, when the PD has finally reached the event horizon of a grown BH.

BHs.

The SPC-configuration accommodates the highest energy scale up to hundreds ZeV in central proto-matter core. For preceding developments of MTBH, and its implications for ultra-high energy (UHE) astrophysics, the interested reader is invited to consult the original papers (Ter-Kazarian, 2014, 2015b, 2016a,b, Ter-Kazarian & Shidhani, 2017). Amongst the subsequent developments, particularly, the UHE-neutrino fluxes from plausible accreting SMBHs closely linking to the 377 AGNs have been computed by (Ter-Kazarian, 2014, 2015b). We concluded that the AGNs are favored as promising pure sources of the high-energy astrophysical neutrinos, up to the UHE, because the computed neutrino fluxes are highly beamed along the plane of accretion disk, and peaked at high energies and collimated in smaller opening angle. The neutrinos are able to stream freely out of SPC, and the bulk of liberated binding energy of proto-matter must be converted into other forms of internal energy rather than being released immediately in the form of escaping neutrinos. That is, while hard to detect, neutrinos have the advantage of representing unique fingerprints of hadron interactions and, therefore, UHE neutrinos may initiate the cascades of UHE cosmic rays via very complex chains of Z-burst interactions. Some part of UHE neutrinos may produce, in accretion disk and in a torus of hot gas surrounding the AGN core, the secondary electrons with huge energies, which, in turn, may give rise a secondary flux of the GeV-TeV gamma-rays. Above said was sharpened by the recent surprising announcement of the first high-energy neutrino event by the IceCube Neutrino Observatory (Collaboration-170922Aalert, 2018). With the very large volume neutrino telescope optimized for the TeV energy range, they have traced a neutrino with the energy approximately 300 TeV that hit their Antarctica-based detector in September 2017 back to its point of origin in a blazar, TXS 0506+056, the 3.7 billion light-years away. This constitutes the first use of a neutrino detector to locate an object in space. In this regard, it will be of vital interest to compute in the framework of MTBH the high-energy astrophysical neutrino fluxes from aforementioned IMBH-candidates too. However, this will subsequently be an interesting topic for the comprehensive study elsewhere.

3. Growth of BH driven by an accretion

One of the key objectives of MTBH is the increase of mass M^{seed} and gravitational radius R_g^{seed} of the seed BH at accretion of outside matter. The matter pulled toward the seed BH (proto-matter core) loses angular momentum through viscous or turbulent processes in an intrinsic accretion disk. Within such a disc, friction would cause angular momentum to be transported outward, allowing matter to fall further inward, thus releasing potential energy and increasing the temperature of the proto-matter. Simultaneously with an increase of seed mass, an infalling matter formes intrinsic proto-matter disk around grown up proto-matter core tapering off faster at reaching out the thin edge of EH. Whereas, the practical measure of a growth of BH is an increase of gravitational radius and mass of the BH:

$$\Delta R_g = R_g - (R_g^{seed})(0) = \Delta R_g^{seed} + \frac{2G}{c^2} M_d, \tag{1}$$

or

$$\Delta R_g = R_g - R_g^{seed} = \frac{2G}{c^2} M_d, \tag{2}$$

where $M_d = M - M^{seed} = \rho_d V_d$, and $R_g^{seed} = (R_g^{seed})_0 + \Delta R_g^{seed}$. The M_d, ρ_d and V_d denote respectively total mass, density and volume of the proto-matter disk. At the value of gravitational radius, $\hat{R}_g$, when the proto-matter disk has finally reached the EH of grown BH, the volume, $\hat{V}_d$, can be calculated in polar coordinates (ρ, z, φ) from the Fig. 4:

$$\hat{V}_d = \hat{V}_d{}^1 - \hat{V}_d{}^2, \tag{3}$$

provided,

$$\hat{V}_d{}^1 = \int_{\rho_0}^{\hat{R}_g} d\rho \int_0^{2\pi} \rho \, d\varphi \int_{-z_1(\rho)}^{z_1(\rho)} dz, \quad \hat{V}_d{}^2 = \int_{\rho_0}^{R_d} d\rho \int_0^{2\pi} \rho \, d\varphi \int_{-z_0(\rho)}^{z_0(\rho)} dz, \tag{4}$$

where $(z_0 - z_1(\rho))/z_0 = (\rho - \rho_0)/(\hat{R}_g - \rho_0)$, and $z_0(\rho) = \sqrt{R_d^2 - \rho^2}$. The integration of (4) gives

$$\hat{V}_d = 4\pi \frac{z_0}{\hat{R}_g - \rho_0} \left[\frac{(\hat{R}_g)^3}{6} - \frac{\hat{R}_g \rho_0^2}{2} - \frac{\rho_0^3}{3} \right] - \frac{4\pi}{3} (R_d^2 - \rho_0^2)^{3/2}, \tag{5}$$

where R_d is the radius of proto-matter core. In approximation at $R_d \ll \hat{R}_g$, we may set $z_0 \simeq \rho_0 \simeq R_d/\sqrt{2}$, such that

$$\hat{V}_d \Big|_{(R_d \ll \hat{R}_g)} \simeq \frac{\sqrt{2}\pi}{3} R_d (\hat{R}_g)^2. \tag{6}$$

Then the mass of proto-matter disk in solar masses can be written

$$\frac{M_d}{M_\odot} \simeq 6.48 \times 10^{-23} \left(\frac{\rho_d}{[\mathrm{g\,cm}^{-3}]} \right) \times \left(\frac{R_d}{[\mathrm{cm}]} \right) \left(\frac{M}{M_\odot} \right)^2. \tag{7}$$

While, the mass of seed BH over that of the Sun reads

$$\frac{M_{BH}^{Seed}}{M_\odot} = \frac{4\pi}{3} \frac{\rho_d R_d^3}{M_\odot} = 2.106 \times 10^{-33} \left(\frac{\rho_d}{[\mathrm{g\,cm}^{-3}]} \right) \left(\frac{R_d}{[\mathrm{cm}]} \right)^3. \tag{8}$$

Thus,

$$m_s = 2.106 \times 10^{-33} \rho r^3 = m(1 - 6.48 \times 10^{-23} \rho r m), \tag{9}$$

where $m_s \equiv M_{BH}^{Seed}/M_\odot$, $\rho \equiv \rho_d/[\mathrm{g\,cm}^{-3}]$, $r \equiv R_d/[\mathrm{cm}]$, and $m \equiv M/M_\odot$. Thence the cubic equation for unknown variable r is written

$$r^3 + 3.077 \times 10^{10} m^2 r - \left(\frac{m}{2.106 \times 10^{-33} \rho} \right) = 0. \tag{10}$$

As far as $p \equiv 3.077 \times 10^{10} m^2 > 0$, there is only one real root, which can be represented in terms of hyperbolic functions, as

$$r = -2\sqrt{\frac{p}{3}} \sinh \left[\frac{1}{3} ar \sinh \left(\frac{3q}{2p} \sqrt{\frac{3}{p}} \right) \right], \tag{11}$$
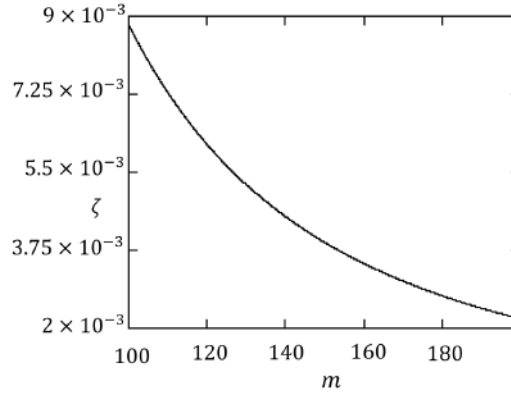
Figure 5. The parameter ζ vs m, at $\rho \simeq 2.6 \times 10^{16}$.

where $q \equiv -m/2.106 \times 10^{-33}\rho$. That is,

$$r = 2.026 \times 10^5 m \sinh\left(\frac{1}{3} ar \sinh \zeta\right), \tag{12}$$

where $\zeta \equiv 2.29 \times 10^{17}/\rho m^2$. Hence the mass of seed BH reads

$$m_s = 1.75 \times 10^{-17}\rho \left[m \sinh\left(\frac{1}{3} ar \sinh \zeta\right)\right]^3. \tag{13}$$

Since the inequality $\zeta \ll 1$ holds for considered IMBH-candidates (see Fig. 6), then by virtue of $r\rho m \simeq 1.54 \times 10^{22}$, as a first order approximation in ζ, the mass of seed BH becomes

$$m_s \simeq 2 \times 10^{-3} m. \tag{14}$$

Therefore,

$$r \simeq 0.983 \times 10^{10} \left(\frac{m}{\rho}\right)^{1/3}. \tag{15}$$

At the best fit $\rho_d \simeq 2.6 \times 10^{16}[\mathrm{gcm}^{-3}]$ (Ter-Kazarian, 2014, 2015b), we have

$$R_d \simeq (0.332[\mathrm{km}])m^{1/3}. \tag{16}$$

4. The neutrino pre-radiation time

To give more credit to this view, next we would like to infer an analytical expression for the BH's 'neutrino pre-radiation time' (PRT), which is referred to as a lapse of time, T_{BH}, from the birth of BH till neutrino radiation - the earlier part of the lifetime. A typical growth rate for a BH is then given by the time required to reach the final mass, M, and gravitational radius, $\hat{R}_g$, when proto-matter disk has finally reached the EH. It is instructive to recast the PRT-scale in the form

$$T_{BH} = \frac{M_d}{\dot{M}}, \tag{17}$$

where $\dot{M}$ is the accretion rate. The order of magnitudes of the accretion rates can be derived if we assume that there is no shortage of the fuel around the BH. Actually, the BHs are fed by the accretion of gas in a process in which a small fraction of the energy of the accreted gas is released in the form of radiation of intensity L. The stars are sufficient to fuel some low luminosity dwarf nuclei: at high densities stellar collisions replenish the central density, and the nuclei can reach higher luminosities. If these conditions are fulfilled, the growth of massive BH can then be accretion-dominated. The mass accretion rate is written (Ter-Kazarian, 2014, 2015b)

$$\dot{M} \equiv \frac{dM}{dt} = \frac{L}{\epsilon\,c^2}, \tag{18}$$

where ϵ is the accretion efficiency to transform the gravitational energy into radiation. According to the canonical Bondi accretion rate, the luminosity has increased as $L \propto \dot{M} \propto M^2$. At some point, the BH growth slows down when approaching to quasar phase, for which the gas maximum rate accretion occurs nearly at the Eddington limit, and radiate at Eddington luminosity, $L_{Edd} = \dfrac{4\pi G M c}{k} = 1.3 \times 10^{38} \left(\dfrac{M}{M_\odot} \right)$ [erg s^{-1}] (above which the radiation pressure prevents the material to fall in), where $k = \sigma_T / m_p$ is the opacity. The $\dot{M}$ is limited by Eddington $\epsilon c^2 \dot{M} < L_{Edd}$. In the same time, it should be emphasized that the possibility of super-Eddington accretion has been also explored theoretically by many authors. A basic reason why this may be feasible is the photon trapping effect on small scales near the BH. That is, in a spherically symmetric accretion flow at a rate much greater than Eddington accretion, the emergent radiation flux is reduced by photon trapping in the optically-thick accreting matter. Such an effect operates when the radial gas in flow speed is faster than the outward photon diffusion speed. The photon trapping effect becomes physically relevant when, so-called, the "trapping radius" $R_{tr} = (k/4\pi c)\dot{M}$ is outside R_g. Note that the Bondi radius is generally much larger than the trapping radius. This idea dates back to the works by (Begelman, 1978, 1979), who constructed a global spherical accretion solution for ionized gas at super-Eddington value. In summary, high accretion rates exceeding the Eddington value are possible but produce intense radiation flux toward the polar directions. These results, however, are valid only as long as a sufficient amount of gas at rates of $\dot{M} \gg \dot{M}_{Edd}$ is supplied from larger scales without being impeded by the strong radiation feedback (see e.g. Inayoshi & Visbal (2019)).

In what follows, for simplicity reasons, the mass supply rate from large scales $\sim \dot{M}_{Edd}$ (precisely tracked as a BH grows by orders of magnitude in mass) is of particular interest to us. Then the Salpeter characteristic time-scale becomes as long as

$$T_s = \epsilon\, t_{Edd} = \epsilon\, \frac{kc}{4\pi G} = \frac{M}{\dot{M}_{Edd}} = \left(\frac{d\,t}{d\,log(M)} \right)_{Edd} = \frac{M\epsilon c^2}{L_{Edd}} = \left(\frac{\epsilon}{0.1} \right) 4.5 \times 10^7 \text{ [yr]}. \tag{19}$$

Thence

$$M\left(\frac{t}{[\text{yr}]} \right) < M(0)\, exp\left(\frac{t}{T_s} \right) = M(0) \times 10^{\frac{t\,log\,e}{T_s}} = M(0) \times 10^{\frac{0.434\,t}{T_s}}. \tag{20}$$

Thus, the characteristic minimum time, t_{min}, which takes at least BH of mass $M(0)$ to grow to mass, M, at the Eddington rate should be

$$t > t_{min} \equiv \frac{T_s}{0.434}\, \log\left(\frac{M}{M(0)} \right) \text{ [yr]} = 1.037 \times 10^8\, \log\left(\frac{M}{M(0)} \right) \text{ [yr]}, \tag{21}$$

where the value of efficiency is taken $\epsilon \simeq 0.1$, like as for high redshift quasars. For a seed mass, say, $M(0) \simeq 10^5 M_\odot$, the accretion of mass at the Eddington rate causes a BH mass to increase in time

$$t_{min} = 1.037 \times 10^8 \times 4 \text{ [yr]} = 4.148 \times 10^8 \text{ [yr]}, \tag{22}$$

to $\simeq 10^9 M_\odot$. This brings one back in time to an epoch when the Universe was very young and galaxies in their infancy. For example, the observation of luminous quasars well in excess of $\simeq 10^{47}$ [erg s^{-1}], at $z \simeq 6$ (Fan & et al., 2001), implies that the first SMBHs with masses $\sim 10^9 M_\odot$ must have formed already in place when the Universe is only 1 [Gyr] old.

Assuming a typical mass-energy conversion efficiency of about $\epsilon \sim 10\%$, in approximation $R_d \ll R_g$ the PRT reads (Ter-Kazarian, 2014, 2015b, Ter-Kazarian et al., 2007)

$$T_{BH} \simeq 0.32 \frac{R_d}{r_{OV}} \left(\frac{M_{BH}}{M_\odot} \right)^2 \frac{10^{39} W}{L_{bol}} \text{ [yr]}. \tag{23}$$

According to (21), PRT-time, T_{BH}, is constrained from the low-limit by

$$T_{BH} > 1.037 \times 10^8\, \log\left(\frac{M}{M^{seed}} \right) \text{ [yr]}. \tag{24}$$

However, unfortunately, the relation (23) cannot be much useful for computing the PRT-scales for IMBHs, because the available observed data of bolometric luminosities of IMBHs at present are scanty. Even though if we use, instead, a proxy of accretion flow and X-ray luminosities of these sources, nevertheless, we certainly

have to touch again upon some rough errors due to data of insufficient accuracy. To overcome this problem, the best way is left perhaps to do stepwise as follows: 1) We at first have to calculate the ratio of PRT-scales of the two SPCs, invoking the relation of the canonical Bondi accretion rate $\dot{M} \propto M^2$ for the central SPC of the given mass M (Ter-Kazarian et al., 2007); 2) Afterwards, we have to calibrate this relation by choosing some SMBH as one of them, which links with a host galaxy with the well observational estimates of bolometric luminosity and mass. Then, the resulting relation should perhaps be of a sufficient accuracy for simulations of the PRT-scales of seeds of alluded IMBH-candidates.

Certainly, let $M(t)$ denotes the sum of masses of grown up seed SPC, $M^{seed}(t)$, and protto-matter disk, $M_d(t)$, at the moment t $(0 \leq t \leq T_{BH})$. Then according to (17), the PRT-scale $T_{BH}(t)$, at moment t, should be

$$T_{BH}(t) = \frac{M_d(t)}{\dot{M}(t)} \propto \frac{M_d(t)}{(M(t))^2} \propto R_d \left(\frac{M(t)}{M(t)} \right)^2 = R_d. \tag{25}$$

For two BHs of given present masses M_1 and M_2, the relation (25), in the limit, yields

$$\frac{T_{BH\,1}}{T_{BH\,2}} = \frac{R_{d\,1}}{R_{d\,2}}. \tag{26}$$

To calibrate (26), let choose the estimates of central SMBH mass, M_2, and PRT-scale, $T_{BH\,2}$, based on properties of the host galaxy, say, Mrk 841 SY1 bulge. The time-scale to drive a large mass $M_2 = 1.26 \times 10^8 \, M_\odot$ to central SMBH, which is a significant fraction of the gas content of a typical galaxy, following (Ter-Kazarian, 2014), is of the order of $T_{BH\,2} \simeq 7.94 \times 10^8$ [yr]. Thereby the simulations give $R_{d\,2} \simeq 2.136 \times 10^5$ [cm] and $M_2^{seed} \simeq 2.88 \times 10^3$. From the relation (26), it is then readily deduced that

$$\tau \equiv \frac{T_{BH}}{[\text{yr}]} \simeq 3.717 \times 10^3 \, r. \tag{27}$$

The (23) can be rewritten

$$\tau \simeq 5.656 \times \left(\frac{10^{45}}{l} \right) m, \tag{28}$$

where $l \equiv L_{bol}/[\text{erg s}^{-1}]$. Comparing (27) with (28), we derive the scaling $M - L$ relation for the mass and bolometric luminosity of IMBHs:

$$l \simeq 1.52 \times 10^{42} \frac{m}{r}. \tag{29}$$

5. The redshift of seed BH

To follow the history of the BH to the present time in the expanding Universe of a general recession of distant galaxies away from us in all directions, the radiation density at the present epoch can be neglected in comparison with the matter density in the Universe. So, the expansion rate of the Universe depends on the matter density, ρ, the cosmological constant, Λ, and the curvature, k, of the space. The expansion rate (Hubble's parameter) of the Universe at any epoch at redshift less than about 1000 can be related to the one at the present epoch by (e.g. Bergström & Goobar (2006)):

$$H(z) = H_0 E(z), \tag{30}$$

where

$$E(z) \equiv \sqrt{[\Omega_M (1+z)^3 + \Omega_K (1+z)^2 + \Omega_\Lambda]}, \tag{31}$$

and $\Omega_\Lambda = \frac{\Lambda}{3 H_0^2}$, $\Omega_K = \frac{-k}{a_0^2 H_0^2}$, $\Omega_M = \frac{\rho}{\rho_{crit}}$, and the critical density is $\rho_{crit} = \frac{3 H^2}{8 \pi G}$. There are only two independent contributions to the energy density

$$\Omega_M + \Omega_\Lambda + \Omega_K = 1. \tag{32}$$

Let the proper time, t, be the temporal measure. This is a convenient time measure because it is the proper time of comoving observers. The lookback time is the time difference between the present epoch, t_0, and the time of an event that happened at the redshift, z. From the definitions of Hubble's parameter and redshift it follows that

$$H = \frac{d}{dt} \log \left(\frac{R(t)}{R_0} \right) = \frac{d}{dt} \ln \left(\frac{1}{1+z} \right) = \frac{-1}{1+z} \frac{dz}{dt}, \tag{33}$$

where R is called the scale factor of the Universe, and increases as the Universe expands in a manner that depends upon the cosmological model selected. Hence, the lookback time from the present, as a function of the time of flight, reads

$$t_0 - t_1(z_1) = H_0^{-1} \int_0^{z_1} \frac{dz'}{(1+z')\sqrt{\Omega_M(1+z')^3 + \Omega_K(1+z')^2 + \Omega_\Lambda}}. \tag{34}$$

Whereas by choosing $t_1 = 0$ (that is $z_1 \to \infty$) in this equation, we obtain the present age of the Universe, τ. For the Einstein-de Sitter Universe ($\Omega_M = 1$, $\Omega_\Lambda = 0$), with from the present epoch $z = 0$ to the beginning of time at $z = \infty$, by integration of (34) one may infer the age of the Universe $\tau = \frac{2}{3H_0}$.

Relating the PRT-scale, T_{BH}, to the redshifts of BH, z, and its seed, z^{seed}, let we place ourselves at the origin of coordinates, $r = 0$, (according to the Cosmological Principle, this is mere convention). Consider a light traveling to us along the $-r$ direction, with angular variables fixed. If the light has left a seed BH, located at r_s, θ_s, φ_s, at time t_s, that happened at the redshift z^{seed}, and it has to reach us at present epoch t_0, at the redshift $z = 0$, then from the definition of the lookback time (34), it follows that

$$H_0(t_0 - t_s(z^{seed})) = \int_0^{z^{seed}} \frac{dz'}{(1+z')\sqrt{\Omega_M(1+z')^3 + \Omega_K(1+z')^2 + \Omega_\Lambda}}. \tag{35}$$

Similar expression can be written for the current BH, located at r_1, θ_1, φ_1, at time t_1, with redshift z:

$$H_0(t_0 - t_1(z)) = \int_0^{z} \frac{dz'}{(1+z')\sqrt{\Omega_M(1+z')^3 + \Omega_K(1+z')^2 + \Omega_\Lambda}}. \tag{36}$$

Subtracting (36) from (35), and taking into account that $t_1 = t_s + T_{BH}$, as seed BH is an object at early times, we obtain

$$H_0(t_0 - t_s(z^{seed})) - H_0(t_0 - t_1(z)) = H_0 T_{BH} = \int_0^{z^{seed}} (\cdots) - \int_0^{z} (\cdots) = \int_z^{z^{seed}} (\cdots). \tag{37}$$

Thus, we arrived to the general relation between the PRT-scale and the redshifts of BH and its seed:

$$H_0 T_{BH} = \int_z^{z^{seed}} \frac{dz'}{(1+z')\sqrt{\Omega_M(1+z')^3 + \Omega_K(1+z')^2 + \Omega_\Lambda}}. \tag{38}$$

As a supplement to the relation (38), we may derive z_s as a function of the quantities z and T_{BH}. Consider a light that travels from a galaxy to a distant observer, both of whom are at rest in comoving coordinates. From radial null-geodesics equation ($ds = 0, d\theta = d\phi = 0$) one derives that if light is emitted from a galaxy at time t and received by us at t_0, it is redshifted z due to the expansion of space, and the overall redshift is therefore given by the Lemaître's important relationship:

$$z = \frac{R(t_0)}{R(t)} - 1. \tag{39}$$

Then, according to the definitions of Hubble's parameter (33), we may write down

$$\begin{aligned} z + 1 &= e^{H(z)(t_0 - t_1)}, \quad \text{for the BH,} \\ z_s + 1 &= e^{H(z_s)(t_0 - t_s)}, \quad \text{for the seed BH.} \end{aligned} \tag{40}$$

Setting $H(z) \simeq H(z_s)$, and taking into account that $t_1 = t_s + T_{BH}$, we obtain

$$\frac{z+1}{z_s+1} = e^{-H(z)(t_1 - t_s)} = e^{-H(z) T_{BH}}. \tag{41}$$

Hence, the function $z_s(z, T_{BH})$ reads

$$z_s = (z+1)e^{H(z) T_{BH}} - 1. \tag{42}$$

5.1. High redshifts

At large redshifts $z >> \Omega_M, \Omega_\Lambda$, only third power of z in the square root in (38) becomes important, and thus we find

$$T_{BH} \simeq \int_z^{z^{seed}} \frac{dz}{H_0\sqrt{\Omega_M}(1+z)^{5/2}} \simeq \frac{2}{3H_0\sqrt{\Omega_M}} \left[\frac{1}{(1+z)^{3/2}} - \frac{1}{(1+z^{seed})^{3/2}} \right]. \tag{43}$$

Therefore, in time to an epoch when the Universe was very young and galaxies in their infancy, the redshift of seed BH reads

$$z^{seed} \simeq \left[\frac{1}{(1+z)^{3/2}} - \frac{3\sqrt{\Omega_M}H_0T_{BH}}{2} \right]^{-2/3} - 1. \tag{44}$$

Using the inverse distance ladder method based on the baryon acoustic oscillations, the DES collaboration (Macaulay & et al., 2018) present a recently improved supernova measurements of the Hubble's constant. They find the value $H_0 = (67.77 \pm 1.30)$[km]/[s]/[Mpc], with the statistical and systematic uncertainties, 68% confidence. This value, incorporating (44) and (28), yield

$$z^{seed} \simeq \left[\frac{1}{(1+z)^{3/2}} - \frac{3\sqrt{\Omega_M}}{2}(39.2 \pm 0.75) \times \frac{M}{M_\odot}\frac{10^{27}\,W}{L} \right]^{-2/3} - 1. \tag{45}$$

By virtue of (27), we may as well obtain

$$z^{seed} \simeq \left[\frac{1}{(1+z)^{3/2}} - \frac{3\sqrt{\Omega_M}}{2} \times (25.76 \pm 0.494) \times 10^{-8}\frac{R_d}{[\text{cm}]} \right]^{-2/3} - 1. \tag{46}$$

5.2. Low redshifts

In time to an epoch when the Universe is old, for low redshifts $z << 1$, in the first-order approximation by the z, from (38), we derive

$$H_0T_{BH} = \int_z^{z^{seed}} \frac{dz}{\sqrt{\Omega_M + \Omega_K + \Omega_\Lambda}} \simeq z^{seed} - z. \tag{47}$$

Hence

$$z^{seed} \simeq z + (25.76 \pm 0.494) \times 10^{-8}\frac{R_d}{[\text{cm}]}. \tag{48}$$

6. A microscopic model building: Research design and methods

The key physical properties of SPC depend very little on the details of concrete SPC-model, because they are a direct consequence of the fundamental features of underlying gravitation theory. We therefore expect that the key properties of non-rotating SPC, even though without being carefully treated, retain for a rotating SPC (App.C) too. Therefore, we have proceeded below in relatively simple way of considering non-rotating black holes, which is quick to estimate the most important conceptual aspects of associated physics, without loss of generality. In going into practical details, we thus adopt the research design and methods of theoretical and numerical preparations discussed recently in (Ter-Kazarian & Shidhani, 2019) and references therein. We attempt to amplify and substantiate the key assertions made in MTBH, and further expose vie working model of the most generic equilibrium configurations of the two classes, with spherical-symmetric distribution of matter in many-phase stratified states. A layering of configuration is a consequence of the onset of different regimes in equation of state. Below we describe stepwise the SPC configurations away from the domain of lower density up to the domain of higher density.

6.1. The I-class SPC configurations

The I-class SPC configurations include:

Domain $\rho < \rho_{drip} = 4.3 \times 10^{11}\,\text{g cm}^{-3}$ - the shell made of cold catalized matter, which is formed after nuclear burning in the density range below neutron drip (ρ_{drip}). Below $10^7\,\text{g cm}^{-3}$, the $^{56}_{26}$Fe nuclei are dominating. In the inner crust, a Coulomb lattice of heavy nuclei co-exist in β- equilibrium with relativistic electrons.

Domain $\rho_{drip} \leq \rho < 4.5 \times 10^{12}\,\text{g cm}^{-3}$ inner crust-the electrons, nuclei and free neutrons co-exist in the medium.

Above the density $\rho > 4.5 \times 10^{12}\,\text{g cm}^{-3}$ the I-class configurations are thought to be composed of two phases of ideal cold n-p-e gas, which is mixture of neutrons, protons and electrons in complete β- equilibrium. The first phase state covers the intermediate density -

Domain $4.5 \times 10^{12}\,\text{g cm}^{-3} \leq \rho < \rho_d = 2.6 \times 10^{16}\,\text{g cm}^{-3}$- which is the regular n-p-e gas in absence of ID. For the intermediate density domain of regular n-p-e gas in absence of ID, according to (**?**), the proton-neutron ratio initially decreases, as the density increases, and reaches a maximum value of 0.0026 at $\rho_0 \simeq 7.8 \times 10^{11} gcm^{-3}$, and afterwards rises monotonically to 1/8 for high densities. Second phase state is-

Domain $\rho > \rho_d$ - the n-p-e proto-matter at short nucleon-nucleon distances $r_{NN} \leq 0.4\,\text{fm}$, in presence of ID.

6.2. The II-class SPC configurations

For the II-class SPC configurations, up to the density range $\rho \leq \rho_{fl} = 4.1 \times 10^{14}\,\text{g cm}^{-3}$, to which the $r_{NN} \leq 1.6\,\text{fm}$ nucloun-nucleon distances correspond, one has the same domains of I-class configurations. Above the density ρ_{fl}, we consider an onset of melting down of hadrons when nuclear matter consequently turns to quark matter. In the domain of $\rho_{fl} \leq \rho < \rho_{as} = m_n\,(0.25\,\text{fm})^3 \simeq 1.1 \times 10^{17}\,\text{g cm}^{-3}$, where m_n is the neutron mass at rest, 0.25 fm is the string thickness, we consider two phase states of string flip-flop regimes (Ter-Kazarian & Shidhani, 2019):

Domain $\rho_{fl} \leq \rho < \rho_d$, to which the distances $0.4\,\text{fm} < r_{NN} \leq 1.6\,\text{fm}$ correspond- the regular string flip-flop, when ID is absent. This is a kind of tunneling effect when the strings joining the quarks stretch themselves violating energy conservation and after touching each other they switch on to the other configuration. We are interested in the individual particle approximation (Hartree approximation), where the Hartree potential is almost linearly proportional to the string length. The Y shape string is the most convenient for calculations, because the center of it almost equals to the center of gravity. At very first, we shall study the classical strings. In analogy to the case of ordinary quark matter, one may readily show that in order to have bound state the rising potential should be a scalar. Similar to ordinary case a red quark searches for the nearest center and joins with it by a string and so on. One simplifies the calculations by assuming that the centers are uniformly distributed with a particle concentration. We assume that quarks have small ordinary mass $m_i \simeq m_u = 5 MeV$. Next, we explore a tunneling effect of quantum fluctuations of string, and the negative potential energy caused by such a quantum jump. The basic technique adopted for calculation of transition matrix element $\widetilde{K}$ is the instanton technique (semi-classical treatment). Due to quantum string flip-flop, an attractive interaction between quarks is presented, when during the quantum transition from a state ψ_1 of energy $\widetilde{E}_1$ to another one ψ_2 of energy $\widetilde{E}_2$, the lowering of energy of system occurs. The quark matter acquires $\Delta \widetilde{E}$ correction to the classical string energy, such that the flip-flop energy lowers the energy of quark matter, consequently by lowering the critical density or critical Fermi momentum. The quark matter acquires $\Delta \widetilde{E}$ correction to the classical string energy, such that the flip-flop energy lowers the energy of quark matter, consequently by lowering the critical density or critical Fermi momentum. If one, for example, looks for the string flip-flop transition amplitude of simple system of $q\bar{q}q\bar{q}$ described by the Hamiltonian $\widetilde{H}$ and invariant action $\widetilde{S}$, then one has

$$< \;\bigl|\!\bigl|\; \Bigl|\; e^{-\widetilde{H}T}\; \Bigr|\; \underset{\sim}{\overset{\sim}{=}} \; > \; = \; < \int [d\widetilde{\sigma}]\, e^{-\widetilde{S}} >, \tag{49}$$

where T is a (imaginary) time interval, $[d\widetilde{\sigma}]$ is the integration over all the possible string motion. The action $\widetilde{S}$ is proportional to the area $\widetilde{A}$ of the surface swept by the strings in the finite region of ID-region of

V_4. The strings are initially in the $\overset{\sim}{=}$ configuration and finally in the $\bigl|\!\bigl|$ configuration. Note that the maximal contribution to the path integral (49) comes from the surface σ_0 of the minimum surface area ('instanton'). A computation of the transition amplitude is strightforward by summing over all the small vibrations around σ_0. Note that string has a finite thickness d, and the width of the area $\Delta\widetilde{A}$ cannot be less than d. This cutoff introduces a factor $\exp(-a_0\,d\,r_{NN})$, (where r_{NN} is the distance between two separated centers) in the amplitude $\widetilde{K}$ resulting in the finite-ranged potential. The interaction energy between two centers has a range of order $2\widetilde{r}$ due to overlap of wave functions. A string thickness d can be estimated to be $0.25 fm$.

Domain $\rho_d \le \rho < \rho_{as}$- the string flip-flop regime in presence of ID at distances $0.25 fm < r_{NN} \le 0.4\,\text{fm}$ - a system is made of quark proto-matter in complete β-equilibrium with rearrangement of string connections joining them.

Domain $\rho > \rho_{as}$- the system is made of quarks in one beg in complete β-equilibrium at presence of ID, under the weak interactions and gluons, including the effects of QCD-perturbative interactions. The QCD vacuum has a complicated structure due to the glueon-glueon interactions. The confinement of quarks is a natural feature of the exercising a pressure B on the surface of the local region of the perturbative vacuum to which quarks are confined. This is just the main idea of phenomenological MIT quark bag model, where quarks are assumed to be confined in a bag. Due to the screening of strong forces, the quarks are considered to be free inside the bag and to interact only in the surface region. The surface energy is estimated to be proportional to quark density. The stability of the hadron is ensured by the vacuum pressure B and surface tension. The surface energy is estimated to be proportional to quark density. In most applications, sufficient accuracy is obtained by assuming that all the quarks are almost massless inside a bag. Now, our purpose is to convert this picture to the medium of quark proto-matter. The quark proto-matter is in overall color singlet ground state, which is a non-interacting relativistic Fermi gas found in the ID-region of the spacetime continuum, at $r_{NN} \le 0.25 fm$. We consider the quark proto-matter of u, d and s flavors, in complete β-equilibrium.

Now, let discuss the QCD interaction effects in approximation at hand, with extension to quark proto-matter. The first effect is the shift of the vacuum energy per unit volume. The bag constant $B \simeq 55 MeV/fm^3$ of the MIT bag model must be added to the kinetic energy density. Including the gluon exchange perturbative interactions the energy density of quark proto-matter is then given by the non-interacting Fermi contribution plus bag constant. The first correction to the free ground state is the ordinary exchange energy corresponding to the second order closed loop diagrams. Next correction is coming up from the sum of different ring diagrams, while the quarks will be taken fully relativistic $m_i \to 0$.

7. The state equation

In our setting we retain the rather concrete proposal of preceding developments of the model of a non-rotating SPC (Ter-Kazarian & Shidhani, 2019) and references therein), without going into the subtleties, as applied to the study of IMBHs. The equations describing the equilibrium SPC include the gravitational and ID field equations, the hydrostatic equilibrium equation, and the state equation of the spherical-symmetric distribution of baryonic-quark matter in many-phase stratified states specified for each domain. We use the Oppenheimer and Volkoff (OV)-units, where a length unit $= 1.368 \times 10^6 cm$, a time unit $= 4.564 \times 10^{-5} s$, a mass unit $= 1.843 \times 10^{34} g$, and energy unit $= 1.656 \times 10^{55} erg$. We also introduce a new variable ν as

$$n_{OV} = 7.96178 \times 10^{55} e^{\nu}, \tag{50}$$

and rewrite the hydrostatic equilibrium equation in the form

$$\nu' = -(s_1 + s_2)\frac{1}{2}\left(\ln g_{00}\right)', \tag{51}$$

where (') means $\partial/\partial r$, $s_1 = \widetilde{P}_{OV}\left(\nu'/P'_{OV}\right)$ and $s_2 = \widetilde{\rho}_{OV}\left(\nu'/\rho'_{OV}\right)$.

The resulting state equations are specified below for each domain step-by-step away from the domain of lower density up to the domain of higher density.

I-Class Conffigurations. The simple semiempirical formula of state equation is given by Harrison and Wheeler (see e.g. Shapiro & Teukolsky (1983)).
Domain: $-27.2 \le \nu < -15.5$,

$$P_{OV} = 4.68 \times 10^{-25}\left(1.93 \times 10^5 \rho_{OV}^{1/3} - 1.44\right)^5 - 2.32 \times 10^{-26},$$
$$s_1 = 1.54 \times 10^{-7}\rho_{OV}^{-1/3} \times \frac{\left[\left(1.93 \times 10^5 \rho_{OV}^{1/3} - 1.44\right)^5 - 1\right]}{\left(1.93 \times 10^5 \rho_{OV}^{1/3} - 1.44\right)^4}, \tag{52}$$
$$s_2 = 6.64 \times 10^{18}\rho_{OV}^{2/3}\left(1.93 \times 10^5 \rho_{OV}^{1/3} - 1.44\right)^{-4}.$$

Domain: $-15.5 \leq \nu < -2.8$,

$$P_{OV} = 0.03\rho_{OV}^{5/4} \left(1 + 2.82 \times 10^{-5}\rho_{OV}^{-1/2}\right)^{-5/6},$$

$$s_1 = \frac{0.08 \left(1 + 2.82 \times 10^{-5}\rho_{OV}^{-1/2}\right)}{\left(1 + 3.99 \times 10^{-5}\rho_{OV}^{-1/2}\right)}, \quad s_2 = 3.17\rho_{OV}^{-1/4}\left(1 + 2.82 \times 10^{-5}\rho_{OV}^{-1/2}\right). \tag{53}$$

Domain: $-2.8 \leq \nu < -0.1$,

$$P_{OV} = 1.79 \times 10^{-5}\rho_{OV}^{2/3}\left(1 + 1.39\rho_{OV}^{1/6})^6\right),$$

$$s_1 = \frac{1.50 \left(1 + 1.40\rho_{OV}^{1/6}\right)}{\left(1 + 3.50\rho_{OV}^{1/6}\right)}, \quad s_2 = 8.36 \times 10^4 \rho_{OV}^{1/3}\left(1 + 1.40\rho_{OV}^{1/6}\right)^{-5} \times \left(1 + 3.50\rho_{OV}^{1/6}\right)^{-1}. \tag{54}$$

Domain: $-0.1 \leq \nu < 8.5$,
-the regular n-p-e gas (ID is absent).
Domain: $8.5 \leq \nu$,
-the state equation of the n-p-e proto-matter reads (Ter-Kazarian & Shidhani, 2019)

$$\widetilde{\rho} = \widetilde{m}_e c^2 \chi(\widetilde{y}_e)/\widetilde{\lambda}_e^3 + \widetilde{m}_p c\chi(\widetilde{y}_p)/\widetilde{\lambda}_p^3 + \widetilde{m}_n c^2 \chi(\widetilde{y}_n))/\widetilde{\lambda}_n^3$$
$$\widetilde{P} = \widetilde{m}_e c^2 \varphi(\widetilde{y}_e)/\widetilde{\lambda}_e^3 + \widetilde{m}_p c^2 \varphi(\widetilde{y}_p)/\widetilde{\lambda}_e^3 + \widetilde{m}_n c^2 \varphi(\widetilde{y}_n)/\widetilde{\lambda}_e^3. \tag{55}$$

For more details and explanation of notational conventions see App.B4.

    II-Class Configurations.
For the II-class configurations, up to the density range $\nu = 8.5$, one has the same domains of I-class configurations. At distances $0.25fm < r_{NN} \leq 0.4fm$, in the
Domain: $8.5 \leq \nu < 9.9$,
the string flip-flop phase state occurs in ID regime (Ter-Kazarian & Shidhani, 2019):

$$\widetilde{\rho} = 3\widetilde{m}c^2\frac{\chi(\widetilde{y})}{\widetilde{\lambda}^3} - 56.29MeV\widetilde{n}_b, \quad \widetilde{P} = 3\widetilde{m}c^2\frac{\varphi(\widetilde{y})}{\widetilde{\lambda}^3}. \tag{56}$$

    Domain: $\nu \geq 9.9$,
-the Λ-like system is made of u, d and s quark protomatter in one bag in complete β-equilibrium under the weak interactions and gluons, including the effects of QCD-perturbative interactions:

$$\widetilde{\rho} = \sum_i \widetilde{m}c_i^2\frac{\chi(\widetilde{y}_i)\widetilde{b}_I}{\widetilde{\lambda}_i^3} + B, \quad \widetilde{P} = \sum_i \widetilde{m}_i c^2\frac{\varphi(\widetilde{y}_i)\widetilde{b}_I}{\widetilde{\lambda}_i^3}, \tag{57}$$

where the quarks will be taken fully relativistic $m_i \to 0$, B is the pressure on the surface of the local region of the perturbative vacuum, to which quarks are confined.

8. Simulations

In this section, we are led to the numerical integration of equations of equilibrium SPC-configurations in presence of ID-mechanism, leading from the center of configuration up to the surface. This is rather technical topic, and it requires care to do correctly. In what follows we only give a brief sketch. We claim that a significant change of properties of spacetime continuum in ID regime is essentially dominated over all the other interaction processes, irrespective to the details of the models in use. Computing the mass of seed BH, the PRT-scale, and the redshift of seed BH, a main idea comes to solving an inverse problem. That is, by the numerous reiterating integrations we determine those required central values of particle concentration $\widetilde{n}(0)$, gravitational $(x_0(0))$ and ID $(x(0))$ fields, for which the integrated total mass of configuration has to be equated to the IMBH mass M given from observations (Ter-Kazarian & Shidhani, 2019). Then, together with all integral characteristics, the radius of proto-matter core, R_d, can also be computed, which is in use in expressions (13), (28), (29), (46) and (48). As it is seen, the BH mass is an important parameter in this study. Of course, there are still large uncertainties in mass estimates collected from the literature of all the observational evidence for 137 IMBH-candidates. As an example, below we present a few comments on the observational mass uncertainties for some of these objects, and their validity or the confidence.
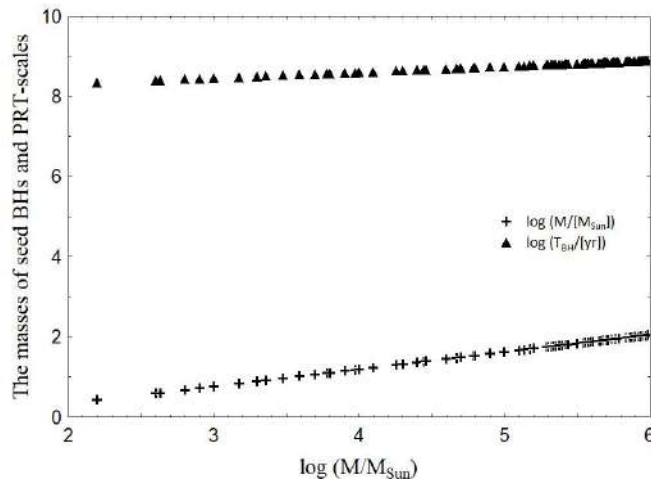
Figure 6. The masses of seed BHs and PRT-scales vs masses of 137 IMBHs.

Kiziltan et al. (2017) show the evidence for a central IMBH with a mass of $2.2^{+1.5}_{-0.8} \, M_\odot$ in 47 Tucanae, which hosts 25 known millisecond pulsars. This IMBH-candidate might be a member of an electromagnetically invisible population of IMBHs that grow into SMBHs in galaxies.

Baldassare & Reines (2015) present optical and X-ray observations of the dwarf galaxy RGG 118 taken with the Magellan Echellette Spectrograph on the 6.5 m Clay Telescope and Chandra X-ray Observatory. Based on Sloan Digital Sky Survey (SDSS) spectroscopy, RGG 118 was identified as possessing narrow emission line ratios indicative of photoionization partly due to AGN. Higher resolution spectroscopy clearly reveals broad H_α emission in the spectrum of RGG 118. They estimate a IMBH mass of $\sim 50,000 \, M_\odot$.

The use of integral field spectroscopy, with the Hubble Space Telescope (HST), to obtain the central velocity-dispersion profile and of photometric data have allowed estimating the BH mass in a dozen more globular clusters by comparing the data to spherical dynamical models. This is the case of another strong IMBH candidate in a globular cluster, ω Centauri, for which claimed the presence of an IMBH of best-fitted mass $(4.7 \pm 1.0) \times 10^4 \, M_\odot$ (Noyola & Gebhardt, 2010, Noyola et al., 2008), while it is reported an upper limit of $(1.2 \pm 1.0) \times 10^4 \, M_\odot$ (Van der Marel & Anderson, 2010). Baumgardt (2017) is also found that the velocity dispersion profile of ω Centauri is best fitted by an IMBH of $10^4 \, M_\odot$.

Using integral-field spectroscopy and HST photometry, Lützgendorf et al. (2013, 2015) reported upper limits on the mass of a putative BH in the globular clusters NGC 1851, NGC 2808, NGC 5694, NGC 5824, and NGC 6093 and predicted the presence of an IMBH of $(3\pm1.0)\times10^3 \, M_\odot$ in NGC 1904, of $(2\pm1.0)\times10^3 \, M_\odot$ in NGC 6266, and of $(2.8 \pm 0.4) \times 10^4 \, M_\odot$ in NGC 6388.

Feldmeier et al. (2009) suspected an IMBH of $(1.5 \pm 1.0) \times 10^3 \, M_\odot$ is also in the globular cluster NGC 5286, and Ibata et al. (2013) reported the possible presence of an IMBH of $\sim 9400 \, M_\odot$ in NGC 6715 (M54), a globular cluster located at the center of the Sagittarius dwarf galaxy.

The natural extension of the well-known $M - \sigma$ relation for galaxies suggests that the typical central velocity dispersions in globular clusters might be associated to the presence of IMBHs with masses of $\sim 10^{3-4} \, M_\odot$ (e.g. Ferrarese & Merritt (2000), Gebhardt & et al. (2000)).

The ULXs have attracted a great deal of observational and theoretical attention, in part because their luminosities suggest that they may harbor IMBHs with an ubiquitous feature of the mass fits of more than $10^2 - 10^4 \, M_\odot$ (H. & Soria, 2011). For overall details regarding this issue, we invite the interested reader to consult further the papers cited in Table 1.

However, for brevity reasons to save space, we put apart the complications of mass uncertainties and retain rather a concrete proposal to proceed in relatively simple way. That is, we select the calculated values of the mass of candidates in the IMBH in order to compare them with the average values of the observational estimates of the mass of the corresponding objects. The masses of seed BHs and PRT-scales vs masses of 137 IMBHs are plotted in Fig.4. The scaling $M-L$ relation for the mass and bolometric luminosity for 137 IMBH-candidates is plotted on the Fig. 5 for 137 IMBH-candidates. The results of the numerical integration of the equations of SPC-configurations of 137 IMBHs, namely the mass of seed BH, the PRT-scale, and the redshift of seed BH, are presented in Table 1. We conclude that for the present masses $\log(M/[\mathrm{M}_\odot]) = 2.20$ to 5.99 of IMBH-candidates, the computed seed masses are ranging from $\log(M^{seed}/[\mathrm{M}_\odot]) = -0.50$ to 3.29, with
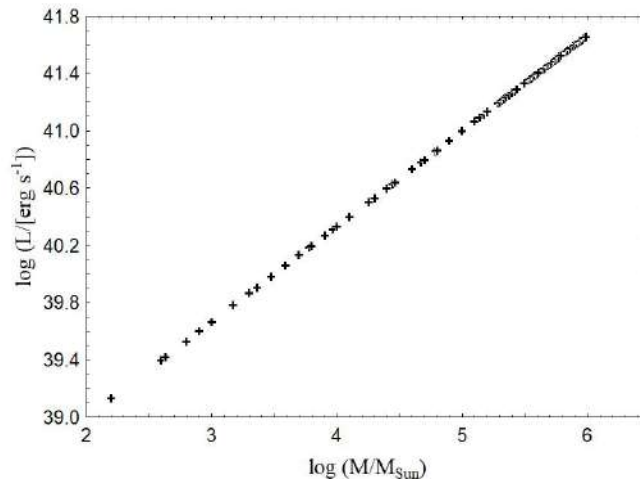
Figure 7. The scaling mass-luminosity relation for 137 IMBH-candidates.

corresponding growth-time scales T_{BH} ranging from $\log(T_{BH}/[\text{yr}]) = 8.82$ to 10.09.

In Table 2, we present the results of computation for the luminosities of 137 IMBHs with the corresponding Eddington luminosities. The luminosities of IMBH-candidates are ranging from $\log(L/[\text{erg s}^{-1}]) = 39.13$ to 41.653.

Finally we note that the growth behavior of IMBH-candidates widely based on the premises of runaway core collapse scenario. The latter has always been a matter of uncertainties because we do not have a thorough understanding of details of accretion physics, say, of the physical properties of invoked relativistic plasma flows outside a horizon, with compact coruscating bright spots due to beaming, or magnetohydrodynamic shocks and reconnection in the inner jet. Distinguishing these possibilities requires spatially resolved images much finer than the horizon size, which could be feasible in the near future. Then it is interesting to compare the accretion method with other methods such as radio timing or even the current research of BH imaging using Event Horizon Telescope. Timing observations provide a useful means to study the properties of space–time around extreme gravity systems, such as BHs. That is, if external tracers lead to an estimated horizon radius, R_g, under a very generic assumption that the object is a BH, then it is possible that finer observations will reveal internal substructures smaller than R_g or flaring events quicker than the time-scale R_g/c. Pulsar timing, therefore, has been identified as a space–time probe because of the high precision achievable in the timing measurements. It is also because of the unique nature of pulsars – highly compact and thus uneasily disrupted, narrow mass range, and for millisecond pulsars, high stability in the rotation rate (a stable, reliable clock). Saxton & et al. (2016) proposed that pulsar timing observations will be able to distinguish between systems with a centrally dense dark matter sphere and conventional galactic nuclei that harbour a SMBH. The lack of a perfect horizon means that the effective strong-lensing silhouette of the central structure may differ significantly from SMBH predictions. Besides, there are some theoretical expectations for swarming of pulsars (and other compact stars) to concentrate in galaxy nuclei (Freitag et al., 2006, Miralda-Escudé & Gould, 2000, Pfahl & Loeb, 2004). So far, one magnetar is known near Sgr A*, and there is debate about how many pulsars might also be discoverable (e.g. Macquart & Kanekar (2015)). Although a thorough comparison is beyond the scope of the present communication, it will be an interesting topic for discussion elsewhere.

9. Concluding Remarks

Deep conceptual and technical problems involved in this contribution provide scope for the arguments discussed, aiming to review the physics of growth behavior of seed BHs at accretion of outside matter. The key mechanism of growth is that the infalling matter formes intrinsic proto-matter disk around grown up proto-matter core tapering off faster at reaching out the thin edge of EH. Below we briefly reflect upon the obtained results. For a broad range of parameters, the numerous reiterating integrations of the state equations of SPC-configurations allow to trace an evolution of the mass assembly history of the BHs to the present time of 137 notable accreting IMBH-candidates. Given the masses and redshifts of IMBH-candidates at present time, collected from the literature, we compute among the others corresponding masses of seed

BHs, the PRT-scales, and their redshifts. In particular, for the present masses $\log(M/[\mathrm{M_\odot}]) = 2.20$ to 5.99 of IMBH-candidates, the computed seed masses are ranging from $\log(M^{seed}/[\mathrm{M_\odot}]) = -0.50$ to 3.29, with corresponding growth-time scales T_{BH} ranging from $\log(T_{BH}/[\mathrm{yr}]) = 8.82$ to 10.09. We derived scaling mass-luminosity relation, by means of which we compute the luminosities of IMBH-candidates ranging from $\log(L/[\mathrm{erg\,s^{-1}}]) = 39.13$ to 41.653.

Table 1. Growth of 137 IMBH-candidates. Column (1) Name of source, (2) log of the IMBH mass at present time over that of the Sun, (3) log of the redshift at present time, (4) log of the radius of proto-matter disk, (5) log of the mass of seed BH over that of the Sun, (6) log of the PRT-scale, (7) log of the redshift of seed BH, (8) log of the time, t_{min}, which takes at least seed BH to grow to mass, M, at the Eddington rate (see (21)). The data of the columns (2) and (3) are taken from the references presented at the end of Table, which marked by superscript in column (1).

Name	$\log\left(\frac{M}{[M_\odot]}\right)$	$\log z$	$\log\left(\frac{R_d}{[cm]}\right)$	$\log\left(\frac{M^{seed}}{[M_\odot]}\right)$	$\log\left(\frac{T_{BH}}{[yr]}\right)$	$\log\left(\frac{t_{min}}{[yr]}\right)$	$\log z^{seed}$
(1)	(2)	(3)	(4)	(5)	(6)	(7)	(8)
NGC 4136[1]	2.20	-2.69	5.25	-0.50	8.82	8.36	-1.77
NGC 3756[1]	2.60	-2.36	5.39	-0.10	8.96	8.43	-1.67
M82-X1[2]	2.63	-3.14	5.40	-0.07	8.97	8.44	-1.75
NGC 3666[1]	2.80	-2.45	5.45	0.10	9.02	8.46	-1.66
NGC 6093[3]	2.90	-4.62	5.49	0.20	9.06	8.48	-1.73
NGC 4062[1]	3.00	-2.60	5.52	0.30	9.09	8.49	-1.66
NGC 5286[4]	3.18	-3.75	5.58	0.48	9.15	8.52	-1.68
NGC 1851[3]	3.30	-2.97	5.62	0.60	9.19	8.53	-1.65
NGC 6266[3]	3.30	-3.63	5.62	0.60	9.19	8.53	-1.66
47 Tucanae (NGC 104)[5]	3.36	-4.21	5.64	0.66	9.21	8.54	-1.66
NGC 1904[3]	3.48	-3.16	5.68	0.78	9.25	8.56	-1.63
NGC 7078[6]	3.59	-3.45	5.72	0.89	9.29	8.57	-1.62
NGC 3344[1]	3.70	-2.71	5.75	1.00	9.32	8.58	-1.58
NGC 5824[2]	3.78	-3.89	5.78	1.08	9.35	8.59	-1.60
IC 467[1]	3.80	-2.16	5.79	1.10	9.36	8.60	-1.49
NGC 2715[1]	3.80	-2.36	5.79	1.10	9.36	8.60	-1.53
NGC 2770[1]	3.80	-2.19	5.79	1.10	9.36	8.60	-1.50
NGC 5694[2]	3.90	-3.16	5.82	1.20	9.39	8.61	-1.57
NGC 6715[7]	3.97	-3.33	5.85	1.27	9.42	8.61	-1.57
NGC 2808[8]	4.00	-3.46	5.85	1.30	9.42	8.62	-1.56
NGC 3600[1]	4.00	-2.62	5.85	1.30	9.42	8.62	-1.53
NGC 4096[1]	4.10	-2.73	5.89	1.40	9.46	8.63	-1.53
G1[9]	4.26	-0.44	5.94	1.56	9.51	8.64	-0.40
NGC 514[1]	4.30	-2.08	5.95	1.60	9.53	8.65	-1.42
NGC 864[1]	4.30	-2.28	5.95	1.60	9.53	8.65	-1.46
NGC 3486[1]	4.30	-2.64	5.95	1.60	9.53	8.65	-1.49
NGC 3003[1]	4.40	-2.31	5.99	1.70	9.56	8.66	-1.45
NGC 3162[1]	4.40	-2.36	5.99	1.70	9.56	8.66	-1.46
NGC 3041[1]	4.40	-2.33	5.99	1.70	9.56	8.66	-1.45
NGC 3198[1]	4.40	-2.64	5.99	1.70	9.56	8.66	-1.48
NGC 6388[10]	4.45	-3.57	6.00	1.75	9.57	8.66	-1.50
RGG119[11]	4.46	-1.26	6.01	1.76	9.58	8.67	-1.06
NGC 3729[1]	4.60	-2.45	6.05	1.90	9.62	8.68	-1.44
NGC 3430[1]	4.60	-2.28	6.05	1.90	9.62	8.68	-1.42
NGC 3726[1]	4.60	-2.54	6.05	1.90	9.62	8.68	-1.45
NGC 4212[1]	4.60	-3.28	6.05	1.90	9.62	8.68	-1.48
NGC 5139[12]	4.67	-3.10	6.08	1.97	9.65	8.69	-1.46
NGC 2276-3c[2]	4.70	-2.09	6.09	2.00	9.66	8.69	-1.38
RGG118[13]	4.70	-1.61	6.09	2.00	9.66	8.69	-1.24
NGC 3780[1]	4.70	-2.10	6.09	2.00	9.66	8.69	-1.38
SDSS J153425.59+040806.7[14]	4.79	-1.40	6.12	2.09	9.69	8.70	-1.13
NGC 2967[1]	4.80	-2.20	6.12	2.10	9.69	8.70	-1.38

Table 1-*cont.*

Name (1)	$\log\left(\frac{M}{[\mathrm{M}_\odot]}\right)$ (2)	$\log z$ (3)	$\log\left(\frac{R_d}{[\mathrm{cm}]}\right)$ (4)	$\log\left(\frac{M^{seed}}{[\mathrm{M}_\odot]}\right)$ (5)	$\log\left(\frac{T_{BH}}{[\mathrm{yr}]}\right)$ (6)	$\log\left(\frac{t_{min}}{[\mathrm{yr}]}\right)$ (7)	$\log z^{seed}$ (8)
SDSS J095418.15+471725.1[15]	4.90	-1.49	6.15	2.20	9.72	8.71	-1.16
NGC 4470[1]	4.90	-2.11	6.15	2.20	9.72	8.71	-1.36
NGC 628[1]	4.90	-2.66	6.15	2.20	9.72	8.71	-1.42
NGC 3433[1]	4.90	-2.04	6.15	2.20	9.72	8.71	-1.34
2XMM J123103.2+110648[16]	5.00	-1.35	6.19	2.30	9.76	8.71	-0.81
2XMM J130543.9+181355[15]	5.00	-0.82	6.19	2.30	9.76	8.71	-0.73
SDSS J122548.86+333248.7[15]	5.00	-2.96	6.19	2.30	9.76	8.71	-1.41
NGC 3938[1]	5.00	-2.54	6.19	2.30	9.76	8.71	-1.39
SDSS J153425.58+040806.6[15]	5.10	-1.40	6.22	2.40	9.79	8.72	-1.11
NGC 3684[1]	5.10	-2.41	6.22	2.40	9.79	8.72	-1.37
NGC 3686[1]	5.10	-2.41	6.22	2.40	9.79	8.72	-1.37
SDSS J091032.80+040832.4[14]	5.14	-1.14	6.23	2.44	9.80	8.73	-0.95
HLX-1[2]	5.17	-1.65	6.25	2.47	9.82	8.73	-1.21
NGC 404[17]	5.18	-3.97	6.25	2.48	9.82	8.73	-1.40
SDSS J160531.84+174826.1[15]	5.20	-1.50	6.25	2.50	9.82	8.73	-1.14
SDSS J144012.70+024743.5[15]	5.20	-1.52	6.25	2.50	9.82	8.73	-1.16
SDSS J101440.21+192448.9[15]	5.20	-1.54	6.25	2.50	9.82	8.73	-1.16
SDSS J105100.64+655940.7[15]	5.20	-1.49	6.25	2.50	9.82	8.73	-1.14
SDSS J120325.66+330846.1[15]	5.20	-1.46	6.25	2.50	9.82	8.73	-1.13
POX 52[20]	5.20	-1.68	6.25	2.50	9.82	8.73	-1.21
2XMM J032459.9-025612[16]	5.29	-1.69	6.28	2.59	9.85	8.74	-1.21
SDSS J112315.75+240205.1[15]	5.30	-1.60	6.29	2.60	9.86	8.74	-1.18
NGC 3185[1]	5.30	-2.39	6.29	2.60	9.86	8.74	-1.34
NGC 4245[1]	5.30	-2.57	6.29	2.60	9.86	8.74	-1.36
NGC 4152[1]	5.30	-2.14	6.29	2.60	9.86	8.74	-1.31
SDSS J024912.86-081525.6[14]	5.32	-1.53	6.29	2.62	9.86	8.74	-1.15
SDSS J082443.28+295923.5[14]	5.33	-1.59	6.30	2.63	9.87	8.74	-1.17
SDSS J163159.59+243740.2[14]	5.33	-1.36	6.30	2.63	9.87	8.74	-1.07
SDSS J102348.44+040553.7[14]	5.34	-1.01	6.30	2.64	9.87	8.74	-0.85
2XMM J213152.8-425130[16]	5.35	-0.96	6.30	2.65	9.87	8.74	-0.82
SDSS J022849.51-090153.7[17]	5.38	-1.14	6.31	2.68	9.88	8.75	-0.94
SDSS J084025.54+181858.9[15]	5.40	-1.82	6.32	2.70	9.89	8.75	-1.24
SDSS J085125.81+393541.7[15]	5.40	-1.39	6.32	2.70	9.89	8.75	-1.08
SDSS J131603.91+292254.0[15]	5.40	-1.42	6.32	2.70	9.89	8.75	-1.09
NGC 3593[1]	5.40	-2.39	6.32	2.70	9.89	8.75	-1.33
NGC 4369[1]	5.40	-2.46	6.32	2.70	9.89	8.75	-1.34
NGC 3507[1]	5.40	-2.49	6.32	2.70	9.89	8.75	-1.34
NGC 2276$_a$[1]	5.40	-2.09	0.37	2.70	8.79	8.57	-1.29
NGC 2776$_b$[1]	5.40	-2.06	6.32	2.70	9.89	8.75	-1.29
NGC 3359[1]	5.40	-2.47	6.32	2.70	9.89	8.75	-1.34
SDSS J083346.04+062026.6[14]	5.42	-0.96	6.33	2.72	9.90	8.75	-0.82
SDSS J114439.34+025506.5[14]	5.43	-0.99	6.33	2.73	9.90	8.75	-0.84
2XMM J120143.6-184857[16]	5.44	-0.80	6.33	2.74	9.90	8.75	-0.70
SDSS J134332.09+253157.7[15]	5.50	-1.54	6.35	2.80	9.92	8.76	-1.14
NGC 4314[1]	5.50	-2.49	6.35	2.80	9.92	8.76	-1.32

Table 1-*cont.*

Name	$\log\left(\frac{M}{[\mathrm{M}_\odot]}\right)$	$\log z$	$\log\left(\frac{R_d}{[\mathrm{cm}]}\right)$	$\log\left(\frac{M^{seed}}{[\mathrm{M}_\odot]}\right)$	$\log\left(\frac{T_{BH}}{[\mathrm{yr}]}\right)$	$\log\left(\frac{t_{min}}{[\mathrm{yr}]}\right)$	$\log z^{seed}$
(1)	(2)	(3)	(4)	(5)	(6)	(7)	(8)
NGC 3596[1]	5.50	-2.40	6.35	2.80	9.92	8.76	-1.32
SDSS J162636.40+350242.0[14]	5.54	-1.47	6.37	2.84	9.94	8.76	-1.10
SDSS J081550.23+250640.9[14]	5.55	-1.14	6.37	2.85	9.94	8.76	-0.93
NGC 4395[18]	5.56	-2.97	6.37	2.86	9.94	8.76	-1.34
SDSS J101627.32-000714.5[14]	5.57	-1.02	6.38	2.87	9.95	8.76	-0.85
SDSS J095151.82+060143.7[14]	5.58	-1.03	6.38	2.88	9.95	8.76	-0.86
NGC 3043[1]	5.60	-2.00	6.39	2.90	9.96	8.76	-1.26
2XMM J134736.4+173404[16]	5.61	-1.35	6.39	2.90	9.96	8.76	-1.04
SDSS J143450.62+033842.5[14]	5.65	-1.55	6.40	2.95	9.97	8.77	-1.13
SDSS J131659.37+035319.8[14]	5.66	-1.34	6.41	2.96	9.98	8.77	-1.04
SDSS J105755.66+482502.0[14]	5.68	-1.14	6.41	2.98	9.98	8.77	-0.92
SDSS J161751.98-001957.4[14]	5.68	-1.24	6.41	2.98	9.98	8.77	-0.98
SDSS J172759.15+542147.0[14]	5.68	-1.00	6.41	2.98	9.98	8.77	-0.83
SDSS J002228.36-005830.6[14]	5.69	-0.98	6.42	2.99	9.99	8.77	-0.82
SDSS J082325.91+065106.4[14]	5.70	-1.14	6.42	3.00	9.99	8.77	-0.9
SDSS J024656.39-003304.8[15]	5.70	-1.34	6.42	3.00	9.99	8.77	-1.03
SDSS J152637.36+065941.6[15]	5.70	-1.42	6.42	3.00	9.99	8.77	-1.07
SDSS J092547.32+050231.6[14]	5.71	-0.90	6.42	3.01	9.99	8.77	-0.76
SDSS J032707.32-075639.3[14]	5.74	-0.81	6.42	3.01	9.99	8.77	-0.70
SDSS J134144.51-005832.9[14]	5.75	-0.83	6.44	3.05	10.01	8.78	-0.71
SDSS J024009.10+010334.5[15]	5.75	-0.71	6.44	3.05	10.01	8.78	-0.61
SDSS J082912.67+500652.3[14]	5.76	-1.36	6.44	3.06	10.01	8.78	-1.04
SDSS J094310.12+604559.1[14]	5.76	-1.13	6.44	3.06	10.01	8.78	-0.91
SDSS 11749.17+044315.5[14]	5.77	-0.97	6.44	3.07	10.01	8.78	-0.81
SDSS J083928.45+082102.3[14]	5.78	-0.89	6.45	3.08	10.02	8.78	-0.75
SDSS J011749.81 -100114.5[14]	5.79	-0.85	6.45	3.09	10.02	8.78	-0.72
SDSS J093829.38+034826.6[14]	5.84	-0.92	6.47	3.14	10.04	8.78	-0.77
UGC 06728[19]	5.85	-2.19	6.47	3.15	10.04	8.78	-1.25
SDSS J131926.52+105610.9[14]	5.86	-1.19	6.47	3.16	10.04	8.78	-0.94
SDSS J103518.74+073406.2[14]	5.87	-1.17	6.48	3.17	10.05	8.78	-0.93
SDSS J144052.60-023506.2[14]	5.89	-1.35	6.48	3.19	10.05	8.79	-1.02
SDSS J015804.75-005221.9[14]	5.90	-1.09	6.49	3.20	10.06	8.79	44.00
SDSS J090320.97+045738.0[14]	5.90	-1.25	6.49	3.20	10.06	8.79	-0.97
SDSS J004042.10-110957.7[15]	5.90	-1.56	6.49	3.20	10.06	8.79	-1.11
SDSS J082422.21+072550.4[14]	5.92	-1.09	6.49	3.22	10.06	8.79	-0.88
SDSS J233837.10-002810.3[14]	5.92	-1.45	6.49	3.22	10.06	8.79	-1.06
SDSS J124035.81-002919.4[14]	5.93	-1.09	6.50	3.23	10.07	8.79	-0.88
SDSS J080907.58+441641.4[14]	5.94	-1.27	6.50	3.24	10.07	8.79	-0.98
SDSS J090431.21+075330.8[14]	5.94	-1.08	6.50	3.24	10.07	8.79	-0.87
SDSS J080629.80+241955.6[14]	5.95	-1.38	6.50	3.25	10.07	8.79	-1.03

Table 1-*cont.*

Name	$\log\left(\frac{M}{[\mathrm{M_\odot}]}\right)$	$\log z$	$\log\left(\frac{R_d}{[\mathrm{cm}]}\right)$	$\log\left(\frac{M^{seed}}{[\mathrm{M_\odot}]}\right)$	$\log\left(\frac{T_{BH}}{[\mathrm{yr}]}\right)$	$\log\left(\frac{t_{min}}{[\mathrm{yr}]}\right)$	$\log z^{seed}$
SDSS J094057.19+032401.2[14]	5.95	-1.22	6.50	3.25	10.07	8.79	-0.95
SDSS J131651.29+055646.9[14]	5.95	-1.26	6.50	3.25	10.07	8.79	-0.97
2XMM J011356.4-144239[16]	5.95	-1.28	6.50	3.25	10.07	8.79	-0.99
SDSS J091449.05+085321.1[14]	5.96	-0.85	6.51	3.26	10.08	8.79	-0.72
SDSS J112526.51+022039.0[14]	5.96	-1.31	6.51	3.26	10.08	8.79	-1.00
SDSS J114343.76+550019.3[14]	5.97	-1.57	6.51	3.27	10.08	8.79	-1.10
SDSS J114633.98+100244.9[14]	5.97	-0.91	6.51	3.26	10.08	8.79	-0.75
SDSS J032515.59+003408.4[14]	5.98	-0.99	6.51	3.28	10.08	8.79	-0.81
SDSS J121518.23+014751.1[14]	5.99	-1.15	6.52	3.29	10.09	8.79	-0.91
SDSS J023310.79-074813.3[15]	5.99	-1.51	6.52	3.29	10.09	8.79	-1.08

(1)- (Graham & Scott, 2013), (2)-(Wang et al., 2015), (3)-(Lützgendorf et al., 2013), (4)- (Feldmeier et al., 2009), (5)- (Kiziltan et al., 2017), (6)- (Gerssen et al., 2002), (7)- (Ibata et al., 2013), (8)-(Lützgendorf et al., 2012), (9)-(Gebhardt et al., 2005), (10)-(Lützgendorf et al., 2015), (11)-(Baldassare & et al., 2016), (12)-(Noyola & Gebhardt, 2010), (13)-(Baldassare & Reines, 2015), (14)-(Xiao et al., 2011), (15)-(Reines et al., 2013), (16)-(Ho & Kim, 2016), (17)-(Nguyen et al., 2017), (18)-(Peterson et al., 2005), (19)-(Bentz et al., 2016), (20)-(Barth et al., 2004)

Table 2. The luminosities of 137 IMBH-candidates. Column (1) Name of source, (2) log of the predicted luminosities, (3) log of the Eddington luminosities.

Name (1)	$\log\left(\frac{L}{[\mathrm{erg\,s^{-1}}]}\right)$ (2)	$\log\left(\frac{L_{Edd}}{[\mathrm{erg\,s^{-1}}]}\right)$ (3)	Name (1)	$\log\left(\frac{L}{[\mathrm{erg\,s^{-1}}]}\right)$ (2)	$\log\left(\frac{L_{Edd}}{[\mathrm{erg\,s^{-1}}]}\right)$ (3)
NGC 4136	39.13	40.29	SDSS J153425.59+040806.7	40.85	42.88
NGC 3756	39.39	40.69	NGC 2967	40.86	42.89
M82-X1	39.42	40.72	SDSS J095418.15+471725.1	40.93	42.99
NGC 3666	39.53	40.89	NGC 4470	40.93	42.99
NGC 6093	39.60	40.99	NGC 628	40.93	42.99
NGC 4062	39.66	41.09	NGC 3433	40.93	42.99
NGC 5286	39.78	41.27	2XMM J123103.2+110648	40.99	43.09
NGC 1851	39.86	41.39	2XMM J130543.9+181355	40.99	43.09
NGC 6266	39.86	41.39	SDSS J122548.86+333248.7	40.99	43.09
47 Tucanae (NGC 104)	39.90	41.45	NGC 3938	40.99	43.09
NGC 1904	39.98	39.98	SDSS J153425.58+040806.6	41.06	43.19
NGC 7078	40.05	40.05	NGC 3684	41.06	43.19
NGC 3344	440.13	41.79	NGC 3686	41.06	43.19
NGC 5824	40.18	41.87	SDSS J091032.80+040832.4	41.09	43.23
IC 467	40.19	41.89	HLX-1	41.11	43.26
NGC 2715	40.19	41.89	NGC 404	41.11	43.27
NGC 2770	40.19	41.89	SDSS J160531.84+174826.1	41.13	43.29
NGC 5694	40.26	41.99	SDSS J144012.70+024743.5	41.13	43.29
NGC 6715	40.31	42.06	SDSS J101440.21+192448.9	41.13	43.29
NGC 2808	40.33	42.09	SDSS J105100.64+655940.7	41.13	43.29
NGC 3600	40.33	42.09	SDSS J120325.66+330846.1	41.13	43.29
NGC 4096	40.39	42.19	POX 52	41.13	43.29
G1	40.50	42.34	2XMM J032459.9-025612	41.19	43.38
NGC 514	40.53	42.39	SDSS J112315.75+240205.1	41.19	43.39
NGC 864	40.53	42.39	NGC 3185	41.19	43.39
NGC 3486	40.53	42.39	NGC 4245	41.19	43.39
NGC 3003	40.59	42.49	NGC 4152	41.19	43.39
NGC 3162	40.59	42.49	SDSS J024912.86-081525.6	41.21	43.41
NGC 3041	40.59	42.49	SDSS J082443.28+295923.5	41.21	43.42
NGC 3198	40.59	42.49	SDSS J163159.59+243740.2	41.21	43.42
NGC 6388	40.63	42.54	SDSS J102348.44+040553.7	41.22	43.43
RGG119	40.64	42.55	2XMM J213152.8-425130	41.23	43.44
NGC 3729	40.73	42.69	SDSS J022849.51-090153.7	41.25	43.47
NGC 3430	40.73	42.69	SDSS J084025.54+181858.9	41.26	43.49
NGC 3726	40.73	42.69	SDSS J085125.81+393541.7	41.26	43.49
NGC 4212	40.73	42.69	SDSS J131603.91+292254.0	41.26	43.49
NGC 5139	40.78	42.76	NGC 3593	41.26	43.49
NGC 2276-3c	40.79	42.79	NGC 4369	41.26	43.49
RGG118	40.79	42.79	NGC 3507	41.26	43.49
NGC 3780	40.79	42.79	NGC 2276	41.26	43.49

Table 2-*cont.*

Name	$\log\left(\frac{L}{[\mathrm{erg\,s^{-1}}]}\right)$	$\log\left(\frac{L_{Edd}}{[\mathrm{erg\,s^{-1}}]}\right)$	Name	$\log\left(\frac{L}{[\mathrm{erg\,s^{-1}}]}\right)$	$\log\left(\frac{L_{Edd}}{[\mathrm{erg\,s^{-1}}]}\right)$
(1)	(2)	(3)	(1)	(2)	(3)
NGC 2776	41.26	43.49	SDSS J131926.52+105610.9	41.57	43.95
NGC 3359	41.26	43.49	SDSS J103518.74+073406.2	41.57	43.96
SDSS J083346.04+062026.6	41.27	43.51	SDSS J144052.60-023506.2	41.59	43.98
SDSS J114439.34+025506.5	41.28	43.52	SDSS J015804.75-005221.9	41.59	43.99
2XMM J120143.6-184857	41.29	43.53	SDSS J090320.97+045738.0	41.59	43.99
SDSS J134332.09+253157.7	41.33	43.59	SDSS J004042.10-110957.7	41.59	43.99
NGC 4314	41.33	43.59	SDSS J082422.21+072550.4	41.61	44.01
NGC 3596	41.33	43.59	SDSS J233837.10-002810.3	41.61	44.01
SDSS J162636.40+350242.0	41.35	43.63	SDSS J124035.81-002919.4	41.61	44.02
SDSS J081550.23+250640.9	41.36	43.64	SDSS J080907.58+441641.4	41.62	44.03
NGC 4395	41.36	43.65	SDSS J090431.21+075330.8	41.62	44.03
SDSS J101627.32-000714.5	41.37	43.66	SDSS J080629.80+241955.6	41.63	44.04
SDSS J095151.82+060143.7	41.38	43.67	SDSS J094057.19+032401.2	41.63	44.04
NGC 3043	41.39	43.69	SDSS J131651.29+055646.9	41.63	44.04
2XMM J134736.4+173404	41.39	43.7	2XMM J011356.4-144239	41.63	44.04
SDSS J143450.62+033842.5	41.40	43.74	SDSS J091449.05+085321.1	41.63	44.05
SDSS J131659.37+035319.8	41.43	43.75	SDSS J112526.51+022039.0	41.63	44.05
SDSS J105755.66+482502.0	41.45	43.77	SDSS J114343.76+550019.3	41.64	44.06
SDSS J161751.98-001957.4	41.45	43.77	SDSS J114633.98+100244.9	41.64	44.06
SDSS J172759.15+542147.0	41.45	43.77	SDSS J032515.59+003408.4	41.65	44.07
SDSS J002228.36-005830.6	41.45	43.78	SDSS J121518.23+014751.1	41.65	44.08
SDSS J082325.91+065106.4	41.46	43.79	SDSS J023310.79-074813.3	41.65	44.08
SDSS J024656.39-003304.8	41.46	43.79			
SDSS J152637.36+065941.6	41.46	43.79			
SDSS J092547.32+050231.6	41.47	43.8			
SDSS J032707.32-075639.3	41.49	43.83			
SDSS J134144.51-005832.9	41.49	43.84			
SDSS J024009.10+010334.5	41.49	43.84			
SDSS J082912.67+500652.3	41.50	43.85			
SDSS J094310.12+604559.1	41.50	43.85			
SDSS 11749.17+044315.5	41.51	43.86			
SDSS J083928.45+082102.3	41.51	43.87			
SDSS J011749.81 -100114.5	41.52	43.88			
SDSS J093829.38+034826.6	41.55	43.93			
UGC 06728	41.56	43.94			

References

Baldassare V., Reines A., 2015, Astrophys. J. Lett. , 809, L14

Baldassare V.F.and Reines A., et al. 2016, Astrophys. J. , 829, 57

Barth A., Ho L., et al. 2004, Astrophys. J. , 607, 90

Baumgardt H., 2017, Mon. Not. R. Astron. Soc. , 464, 2174

Begelman M., 1978, Mon. Not. R. Astron. Soc. , 84, 53

Begelman M., 1979, Mon. Not. R. Astron. Soc. , 187, 237

Bentz M., Batiste M., et al. 2016, Commun. Math. Phys., 273, 217

Bergström L., Goobar A., 2006, Cosmology and Particle Astrophysics, 2nd edn. Springer,ISBN 3-540-32924-2

Chen J.-H., Shen R.-F., 2018, Astrophys. J. , 867, 8

Collaboration-170922Aalert I., 2018, Science

Datt S., 1938, Zs. f. Phys., 108, 108

Dubrovin B., et al. 1986, Contemporary Geometry. Nauka, Moscow

Fan X., et al. 2001, Astron. J. , 121, 54

Feldmeier A., Lützgendorf N., et al. 2009, Astron. Astrophys. , 554, A63

Ferrarese L., Merritt D., 2000, Astrophys. J. Lett. , 539, L9

Fragione G., Ginsburg I., Kocsis B., 2018, Astrophys. J. , 856, 16

Freitag M., Amaro-Seoane P., Kalogera V., 2006, Astrophys. J. , 649, 91

Gallerani S., Fan X., Maiolino R., Pacucci F., 2017, Proc. Astron. Soc. Aust. , 34, 19

Gebhardt K., et al. 2000, Astrophys. J. Lett. , 539, L13

Gebhardt K., Rich R., Ho L., 2005, Astrophys. J. , 634, 1093

Gerssen J., van der Marel R., et al. 2002, Astrophys. J. , 124, 3270

Giambo R., Giannoni F., Magli G., Piccione P., 2004, Gen. Relativ. Gravit., 36, 1279

Goswami R., Joshi P., 2002, Class. Quantum Grav., 19, 5229

Graham A., Scott N., 2013, Astrophys. J. , 764, 151

H. F., Soria R., 2011, New Astron. Rev., 55, 166

Harrison E. R., 2018, Astrophys. J. , 867, 7

Ho L., Kim M., 2016, Astrophys. J. , 821, 48

Ibata R., Bellazzini M., et al. 2013, Astrophys. J. , 699, L69

Inayoshi K., Visbal E.Haiman Z., 2019, Ann. Rev. Astron. Astrophys. , 58, 1

Johnson J., Haardt F., 2016, PASA, 33, e007

Joshi P., Malafarina D., 2011, Int. J. Mod. Phys. D, 20, 2641

Joshi P., Malafarina D., 2013, Gen. Re. Grav., 45, 305

Kaaret P., Feng H., 2017, Ann. Rev. Astron. Astrophys. , 55, 303

Katz H., Sijacki D., Haehnelt M., 2015, Mon. Not. R. Astron. Soc. , 451, 2352

Kiziltan B., Baumgardt H., Loeb A., et al. 2017, Nature, 542, 203

Koliopanos F. e. a., 2017, Astron. Astrophys. , 601, A20

Koliopanos F., 2018, in the XIIth Workshop on Multifrequency Behaviour of High Energy Cosmic Sources. pp Palermo, Italy–2017

Laporte N., Ellis R. S., Boone F., et al. 1969, Riv. Nuovo Cimento, 1, 252

Latif M., Ferrara A., 2016, Proc. Astron. Soc. Aust. , 33, e051

Latif M., Schleicher D., 2018, Formation of the First Black Holes. World Scienti
    c Publishing Co., Singapore

Lin D., Strader J., et al. 2018, Nature Astronomy, 2, 656

Lützgendorf N., Kissler-Patig M., et al. 2012, Astron. Astrophys. , 542, A129

Lützgendorf N., Kissler-Patig M., et al. 2013, Astron. Astrophys. , 552, A49

Lützgendorf N., Gebhardt K., et al. 2015, Astron. Astrophys. , 581, A1

Macaulay E., et al. 2018, DES collaboration) (2018). "First Cosmological Results using Type Ia Supernovae from the Dark Energy Survey: Measurement of the Hubble Constant", arXiv:1811.02376 [astro-ph.CO]

Macquart J.-P., Kanekar N., 2015, Astrophys. J. , 805, 172

Mezcua M., 2017, Intl. J. of Mod. Phys. D, 26, Issue 11, id. 1730021

Miralda-Escudé J., Gould A., 2000, Astrophys. J. , 545, 847

Nguyen D., Seth A., et al. 2017, Astrophys. J. , 836, 237

Noyola E., Gebhardt K. e. a., 2010, Astrophys. J. Lett. , 719, L60

Noyola E., Gebhardt K., Bergmann M., 2008, Astrophys. J. , 676, article id. 1008

Oppenheimer J., Snyder H., 1939, Phys. Rev., 56, 455

Perera B., Stappers B. e. a., 2018, in Proc. of the IAU Symposium. p. 247

Perera B., Stappers B., et al. 2017, Mon. Not. R. Astron. Soc. , 468, Issue 2, 2114

Peterson B., Bentz M., et al. 2005, Astrophys. J. , 632, 799

Pfahl E., Loeb A., 2004, Astrophys. J. , 615, 253

Pontryagin L., 1984, Continous Groups. Nauka, Moscow

Reines A., Greene J., Geha M., 2013, Astrophys. J. , 775, 116

Robinson D., 1975, Phys. Rev. Lett. , 34, 901

Sakurai Y., Yoshida N., et al. 2017, Mon. Not. R. Astron. Soc. , 472, 1677

Saxton C., et al. 2016, Mon. Not. R. Astron. Soc. , 461, 4295

Shapiro S., Teukolsky S., 1983, Black Holes, White Dwarfs, and Neutron Stars. A Wiley-Intercience Publication, New York

Soria R., Musaeva A., et al. 2017, Mon. Not. R. Astron. Soc. , 469, Issue 1, 886

Takekawa S., Oka T., Iwata Y., Tsujimoto S., Nomura M., 2019, Astrophys. J. Lett. , 871, L1

Ter-Kazarian G., 2010, Astrophys. Space. Sci. , 327, 91

Ter-Kazarian G., 2011, Class. Quantum Grav., 28, 055003

Ter-Kazarian G., 2012, Advances in Mathematical Physics, 2012, 1

Ter-Kazarian G., 2014, Astrophys. Space. Sci. , 349, 919

Ter-Kazarian G., 2015a, Physics Research International, 2015, Article ID 152846, 1

Ter-Kazarian G., 2015b, J. of Astrophysics, 2015, Article ID 205367, 1

Ter-Kazarian G., 2016a, Advances in Astrophys., 1, issue 3, 21

Ter-Kazarian G., 2016b, Astrophys. Space. Sci. , 361, issue 1, 20

Ter-Kazarian G., Shidhani S., 2017, Advances in Astrophys., 2, No.3, 162

Ter-Kazarian G., Shidhani S., 2019, Astrophys. Space. Sci. , 364, Issue 10, article id. 165, 23pp

Ter-Kazarian G., Shidhani S., Sargsyan L., 2007, Astrophys. Space. Sci. , 310, 93

Van der Marel R., Anderson J., 2010, Astrophys. J. , 710, 1063

Villas da Rocha J., Wang A., 2000, Class. Quantum Grav., 17, 2589

Wang S., Liu J., Bai Y., Guo J., 2015, Astrophys. J. Lett. , 812, L34

Webb N. e. a., 2017, Astron. Astrophys. , 5602, id.A103, 9

Woods T., Agarwal B., Bromm V., Bunker A., et al. 2019, Proc. Astron. Soc. Aust. , 36, e027

Xiao T., Barth A., Greene J., et al. 2011, Astrophys. J. , 739, 28

Appendices

Appendix A   Outline of key points of underlying gravitation theory

In this section we recount some of the highlights behind of underlying gravitation theory, which is the crux of the theoretical framework of MTBH. Much use has been made of the language of fundamental geometric structure - *distortion gauge induced fiber-bundle*, provided with the spacetime deformation/distortion- framework (Ter-Kazarian, 2011, 2014, 2015b). In the framework of spacetime deformation theory (Ter-Kazarian, 2011, 2015b) and references therein, we consider a smooth deformation map $\Omega : M_4 \to \widetilde{\mathcal{M}}_4$, written in terms of the *world-deformation* tensor (Ω), the general ($\widetilde{\mathcal{M}}_4$) and flat ($M_4$) smooth differential 4D-manifolds. A following notational conventions will be used throughout the appendices. All magnitudes related to the space, $\widetilde{\mathcal{M}}_4$, will be denoted with an over $'\sim'$. We use the Greek alphabet ($\mu, \nu, \rho, ... = 0, 1, 2, 3$) to denote the holonomic world indices related to $\widetilde{\mathcal{M}}_4$, and the second half of Latin alphabet ($l, m, k, ... = 0, 1, 2, 3$) to denote the world indices related to M_4. The tensor, Ω, can be written in the form $\Omega = \widetilde{D} \, \widetilde{\psi} \, (\Omega^m_l = \widetilde{D}^m_\mu \, \widetilde{\psi}^\mu_l)$, where the DC-members are the invertible distortion matrix $\widetilde{D} (\widetilde{D}^m_\mu)$ and the tensor $\widetilde{\psi} (\widetilde{\psi}^\mu_l \equiv \partial_l \widetilde{x}^\mu$ and $\partial_l = \partial/\partial \, x^l)$. The principle foundation of the *world-deformation* tensor (Ω) comprises the following two steps: 1) the basis vectors e_m at given point ($p \in M_4$) undergo the *distortion* transformations by means of $\widetilde{D}$; and 2) the diffeomorphism $\widetilde{x}^\mu(x) : M_4 \to \widetilde{M}_4$ is constructed by seeking a new holonomic coordinates $\widetilde{x}^\mu(x)$ as the solutions of the first-order partial differential equations. Namely,

$$\widetilde{e}_\mu = \widetilde{D}^l_\mu \, e_l, \quad \widetilde{e}_\mu \, \widetilde{\psi}^\mu_l = \Omega^m_l e_m, \tag{58}$$

where the conditions of integrability, $\partial_k \, \psi^\mu_l = \partial_l \, \psi^\mu_k$, and non-degeneracy, $\|\psi\| \neq 0$, necessarily hold (Dubrovin & et al., 1986, Pontryagin, 1984). For reasons that will become clear in the sequel, next we write the norm $d\widetilde{s} \equiv i\widetilde{d}$ (see App.B) of the infinitesimal displacement $d\widetilde{x}^\mu$ on the $\widetilde{\mathcal{M}}_4$ in terms of the spacetime structures of M_4:

$$i\widetilde{d} = \widetilde{e} \, \widetilde{\vartheta} = \widetilde{e}_\mu \otimes \widetilde{\vartheta}^\mu = \Omega^m_l \, e_m \otimes \vartheta^l \in \widetilde{\mathcal{M}}_4. \tag{59}$$

A deformation $\Omega : M_4 \to \widetilde{\mathcal{M}}_4$ comprises the following two 4D deformations $\overset{\circ}{\Omega}: M_4 \to V_4$ and $\overset{\smallsmile}{\Omega} : V_4 \to \widetilde{M}_4$, where V_4 is the semi-Riemannian space, $\overset{\circ}{\Omega}$ and $\overset{\smallsmile}{\Omega}$ are the corresponding *world deformation* tensors.

In what follows, we restrict ourself to consider only the simplest spacetime deformation map, $\Omega : M_4 \to V_4$, where V_4 is the 4D semi-Riemannian space. The quantities denoted by wiggles here refer to V_4 space, but the quantities referring to flat M_4 space are left without wiggles as previously. Given the principal fiber bundle $\widetilde{P}(V_4, G_V; \widetilde{s})$ with the structure group G_V, the local coordinates $\widetilde{p} \in \widetilde{P}$ are $\widetilde{p} = (\widetilde{x}, U_V)$, where $\widetilde{x} \in V_4$ and $U_V \in G_V$, the total bundle space $\widetilde{P}$ is a smooth manifold, the surjection $\widetilde{s}$ is a smooth map $\widetilde{s} : \widetilde{P} \to V_4$. The collection of matter fields of arbitrary spins $\widetilde{\Phi}(\widetilde{x})$ take values in standard fiber over $\widetilde{x} : \widetilde{s}^{-1}(\widetilde{\mathcal{U}}_i) = \widetilde{\mathcal{U}}_i \times \widetilde{F}_{\widetilde{x}}$. The action of the structure group G_V on $\widetilde{P}$ defines an isomorphism of the Lie algebra $\widetilde{\mathfrak{g}}$ of G_V onto the Lie algebra of vertical vector fields on $\widetilde{P}$ tangent to the fiber at each $\widetilde{p} \in \widetilde{P}$ called fundamental.

We generalize the standard gauge scheme by exploring a new special type of *distortion* gauge field. Then we also consider the principle fiber bundle, $P(M_4, U^{loc}; s)$, with the base space M_4, the structure group U^{loc} and the surjection s. The matter fields $\Phi(x)$ take values in the standard fiber which is the Hilbert vector space where a linear representation $U(x)$ of group U^{loc} is given. This space can be regarded as the Lie algebra of the group U^{loc} upon which the Lie algebra acts according to the law of the adjoint representation: $a \leftrightarrow ad \, a \ \Phi \to [a, \Phi]$. We assume that a distortion massless gauge field $a(x) (\equiv a_n(x))$ has to act on the external spacetime groups. This field takes values in the Lie algebra of the abelian group U^{loc}. We build up the world-deformation tensor, $\Omega(F) = D(a) \, \psi(a)$. We connect the structure group G_V, further, to the nonlinear realization of the Lie group G_D of the distortion of extended space $M_6(\to \widetilde{M}_6)$, underlying the M_4.

The nonlinear realization technique or the method of phenomenological Lagrangians provides a way to determine the transformation properties of fields defined on the quotient space. We treat the distortion group G_D and its stationary subgroup $H = SO(3)$, respectively, as the dynamical group and its algebraic subgroup. The fundamental field is distortion gauge field (a) and, thus, all the fundamental gravitational structures in fact - the metric as much as the coframes and connections - acquire a *distortion-gauge induced*

theoretical interpretation. We study the geometrical structure of the space of parameters in terms of Cartan's calculus of exterior forms and derive the Maurer-Cartan structure equations, where the distortion fields (a) are treated as the Goldstone fields.

Addressing the rearrangement of vacuum state, in realization of the group G_V we implement the abelian local group, $U^{loc} = U(1)_Y \times \overline{U}(1) \equiv U(1)_Y \times diag[SU(2)]$, on the space M_6 (spanned by the coordinates η), with the group elements of $exp\left[i\frac{Y}{2}\theta_Y(\eta)\right]$ of $U(1)_Y$ and $exp\left[iT^3\theta_3(\eta)\right]$ of $\overline{U}(1)$. This has two generators, the third component T^3 of isospin $\vec{T}$ related to the Pauli spin matrix $\frac{\vec{\tau}}{2}$, and hypercharge Y implying $Q^d = T^3 + \frac{Y}{2}$, where Q^d is the *distortion charge* operator assigning the number -1 to particles, but +1 to anti-particles. The group U^{loc} entails two neutral gauge bosons of $\overline{U}(1)$, or that coupled to T^3, and of $U(1)_Y$, or that coupled to the hypercharge Y. Spontaneous symmetry breaking can be achieved by introducing the neutral complex scalar Higgs field. Minimization of the vacuum energy fixes the non-vanishing vacuum expectation value (VEV), which spontaneously breaks the theory, leaving the $U(1)_d$ subgroup intact, i.e. leaving one Goldstone boson. Consequently, the left Goldstone boson is gauged away from the scalar sector, but it essentially reappears in the gauge sector providing the longitudinally polarized spin state of one of gauge bosons that acquires mass through its coupling to Higgs scalar. Thus, the two neutral gauge bosons were mixed to form two physical orthogonal states of the massless component of *distortion* field, (a) ($M_a = 0$), which is responsible for gravitational interactions, and its massive component, ($\bar{a}$) ($M_{\bar{a}} \neq 0$), which is responsible for the ID-regime. Hence, a substantial change of the properties of the spacetime continuum besides the curvature may arise at huge energies. Hence, a substantial change of the properties of the spacetime continuum besides the curvature may arise at huge energies. The theory is renormalizable, because gauge invariance gives conservation of charge, also ensures the cancelation of quantum corrections that would otherwise result in infinitely large amplitudes. Without careful thought we expect that in this framework the renormalizability of the theory will not be spoiled in curved space-time too, because, the infinities arise from ultra-violet properties of Feynman integrals in momentum space which, in coordinate space, are short distance properties, and locally (over short distances) all curved space-time look like maximally symmetric (flat) space.

Appendix B Field equations of non-spinning SPC in ID regime

The field equations of non-spinning SPC follow at once from the total gauge invariant Lagrangian in terms of Euler-Lagrange variations, respectively on both the 4D semi-Riemannian space $V_4 = \widetilde{R}^3 \oplus \widetilde{R}^0$, and the 4D flat space $M_4 = R^3 \oplus R^0$ (Ter-Kazarian & Shidhani, 2019). We are interested in the case of a 1D spherical-symmetric gravitational field $(a_0(r))$, $(r \in R^3)$, in presence of 1D space-like ID-field $(\bar{a}(r))$. In the case at hand, one has the group of motions $SO(3)$ with 2D space-like orbits S^2 where the standard coordinates are $\widetilde{\theta}$ and $\widetilde{\varphi}$. The stationary subgroup of $SO(3)$ acts isotropically upon the tangent space at the point of sphere S^2 of radius $\widetilde{r}$. So, the bundle $p: V_4 \to \widetilde{R}^2$ has the fiber $S^2 = p^{-1}(\widetilde{x})$, $\widetilde{x} \in V_4$ with a trivial connection on it, where $\widetilde{R}^2$ is the quotient-space $V_4/SO(3)$.

Considering the equilibrium configurations of degenerate baryonic-quark matter, we assume an absence of transversal stresses and the transference of masses in the space V_4:

$$T_1^1 = T_2^2 = T_3^3 = -\widetilde{P}(\widetilde{r}), \quad T_0^0 = -\widetilde{\rho}(\widetilde{r}), \tag{60}$$

where T_ν^μ is taken to denote the components of energy stress tensor.

The equations of gravitation, $x_0 := \text{æ}a_0$, and ID, $x := \text{æ}\bar{a}$, fields can be written in Feynman gauge as follows (Ter-Kazarian, 2014, 2015b):

$$\begin{aligned}
\Delta x_0 &= -\text{æ}^2 \left\{ \frac{1-x_0}{(1-x_0)^2+x^2}\widetilde{\rho}(\widetilde{r}) + \frac{1+x_0}{(1-x_0)^2+x^2}\widetilde{P}(\widetilde{r}) \right\}, \\
\left(\Delta - \lambda_a^{-2}\right)x &= \text{æ}^2 x \left\{ \frac{\widetilde{\rho}(\widetilde{r})}{(1-x_0)^2+x^2} - \frac{\widetilde{P}(\widetilde{r})}{(1-x_0)^2+x^2} \right\} \times \theta\left(\lambda_a - n^{-1/3}\right).
\end{aligned} \tag{61}$$

Reviewing notations æ is the coupling constant relating to the Newton gravitational constant (G) as $\text{æ} = 8\pi G/c^4$, $\widetilde{P}(\widetilde{r})$ and $\widetilde{\rho}(\widetilde{r})$ ($\widetilde{r} \in \widetilde{R}^3$) are taken to denote the internal pressure and macroscopic density of energy defined in proper frame of reference that is being used, $\widetilde{n}$ is the distorted concentration of particles, r is the radius-vector defined on flat space R^3, $\Delta \equiv \partial^2/\partial r^2$, $\theta(t)$ is the step function $\theta(t) = \begin{cases} 1 & t \geq 0 \\ 0 & t < 0 \end{cases}$, and λ_a is the Compton length of the ID-field: $\lambda_a = \hbar/m_a c \simeq 0.4\,\text{fm}$. A diffeomorphism $\widetilde{r}(r): M_4 \to V_4$ is

defined as $r = \widetilde{r} - R_g/4$, where R_g is the gravitational radius of distribution of matter, $R_g = 2GM/c^2 = 2.95 \times 10^5 \, M/M_\odot$ cm.

In the framework of MTBH, more profound geometrical structures enable an insight to explore a novel aspects expected from a significant change of properties of spacetime continuum in ID-regime. This manifests its virtues below the ID-threshold length, yielding the transformations of Poincaré generators of translations (Ter-Kazarian & Shidhani, 2019), which, in turn, lead to the phase transition of each particle located in the ID-region:

$$\widetilde{E} = E, \quad \widetilde{P}_{1,2} = P_{1,2}\cos\widetilde{\theta}_3, \quad \widetilde{P}_3 = P_3 - \tan\widetilde{\theta}_3 \, mc,$$

$$\widetilde{m} = \left| \left(m - \tan\widetilde{\theta}_3 \frac{P_3}{c}\right)^2 + \sin^2\widetilde{\theta}_3 \frac{P_1^2 + P_2^2}{c^2} - \tan^2\widetilde{\theta}_3 \frac{E^2}{c^4} \right|^{\frac{1}{2}}, \tag{62}$$

where $E, \vec{P}, m$ and $\widetilde{E}, \widetilde{\vec{P}}, \widetilde{m}$ are, respectively, ordinary and distorted energy, momentum and mass at rest, and $\tan\widetilde{\theta}_3 = -x, \quad \widetilde{\theta}_1 = \widetilde{\theta}_2 = 0$. Consequently, a whole matter found in the ID-region of spacetime continuum is undergone phase transition of II-type.

The explicit form of the line element from the outside of configuration $\widetilde{r} > \widetilde{r}_b$, where $\widetilde{r}_b$ is the boundary of distribution of matter, reads

$$d\,s^2 = (1 - x_0)^2 d\widetilde{t}^2 - (1 + x_0)^2 d\widetilde{r}^2 - \widetilde{r}^2(\sin^2\theta d\,\varphi^2 + d\,\theta^2). \tag{63}$$

Given the state equation, the hydrostatic equilibrium equation can be integrated. While an integration constant is determined from the condition of matching of internal and external metrics. Hence

$$g_{00}(r_f) = (1 - \frac{R_g}{2r_b})^2 \exp\left[\int_0^{\widetilde{P}} \frac{2\widetilde{P}}{\widetilde{P} + \widetilde{\rho}}\right]. \tag{64}$$

To make the reader fully understood, it is worthwhile before proceeding further to discuss in more detail one principle issue in use. Recall that according to the fundamental idea, conceived in the framework of GR, the EH is impenetrable barrier for crossing from inside the BH, because of a singularity arisen at Schwarzschild radius. But this barrier disappears in the framework of MTBH, when a matter, located in ID-region of the spacetime continuum, has undergone phase transition of II-type and, thus, it becomes a proto-matter. To obtain some feeling about this phenomena, note that (according to the field equations (61)), a singularity at intersection of proto-matter disk with the event horizon disappears where a massive component of ID-field is not zero, and hence the crossing event horizon from inside of BH at such conditions is allowed.

B.1   The n-p-e baryonic proto-matter

The state equation of baryonic proto-matter can be derived usually from the minimization of energy density incorporated with the conservation laws of baryonic and electric charges. The state equation of one-component degenerate Fermi proto-matter can be written (Ter-Kazarian, 2014, 2015b) and references therein:

$$\widetilde{\rho} = \widetilde{m}c^2 \frac{\chi(\widetilde{y})}{\widetilde{\lambda}^3} + \widetilde{n}_b \widetilde{U}(\widetilde{n}_b), \quad \widetilde{P} = \widetilde{m}c^2 \frac{\varphi(\widetilde{y})}{\widetilde{\lambda}^3} + \widetilde{n}_b^2 \frac{\partial \widetilde{U}(\widetilde{n}_b)}{\partial \widetilde{n}_b}, \tag{65}$$

where $\widetilde{U}(\widetilde{n}_b)$ is the potential energy per baryon. The following notational conventions are used throughout:

$$\begin{aligned}
&\chi(\widetilde{y}) = \frac{1}{8\pi^2}\left\{\widetilde{y}(1 + \widetilde{y}^2)^{1/2}(1 + 2\widetilde{y}^2) - \left[\widetilde{y} + (1 + (1 + \widetilde{y}^2)^{1/2}\right]\right\}, \\
&\varphi(\widetilde{y}) = \frac{1}{8\pi^2}\left\{\widetilde{y}(1 + \widetilde{y}^2)^{1/2}(\frac{2}{3}\widetilde{y}^2 - 1) + \ln\left[\widetilde{y} + (1 + (1 + \widetilde{y}^2)^{1/2}\right]\right\}, \quad \widetilde{m} = (|\,\eta\,|)^{1/2}, \\
&\eta = 1 - x^2 - xy/\sqrt{3} - y^2 x^4 / 6(1 + x^2), \\
&y = P_F/mc = (3\pi^2)^{1/3}\lambda n^{1/3}, \\
&\widetilde{y} = \widetilde{P}_F/\widetilde{m}c = (3\pi^2)^{1/3}\widetilde{\lambda}\widetilde{n}^{1/3}, \quad \widetilde{P}_F = P_F\zeta^{1/2}, \\
&\zeta = y^2\left[1 - 2x^2/3(1 + x^2)\right] + 2xy/\sqrt{3} + x^2,
\end{aligned} \tag{66}$$

provided, $\widetilde{P}_F$ and P_F are distorted and ordinary Fermi momenta, $\widetilde{n}$ is the distorted concentration of particles, $\lambda = \hbar/mc, \quad \widetilde{\lambda} = \hbar/\widetilde{m}c$. To simplify the problem in (66), we approximately set $P_1 = P_2 = P_3 = P/\sqrt{3} = |\,P\,|/\sqrt{3}, \ P/mc \simeq x/2$.

Suppose that the free neutrons, protons and electrons of $n - p - e$ proto-matter, at high densities $\rho \geq \rho_d$, are in complete β-equilibrium. That is, $\widetilde{\mu}_e + \widetilde{\mu}_p = \widetilde{\mu}_n$ and $\widetilde{\mu}_\nu = \mu_\nu = 0$. Then,

$$\widetilde{m}_e(1 + y_e)^{1/2} + \widetilde{m}_p(1 + y_p)^{1/2} = \widetilde{m}_n(1 + y_n)^{1/2}, \tag{67}$$

where m_e, m_p and m_n are the ordinary masses at rest of electron, proton and neutron. The electrical charge neutrality implies $\widetilde{n}_e = \widetilde{n}_p$, i.e. $\widetilde{m}_e \widetilde{y}_e = \widetilde{m}_p \widetilde{y}_p$. By virtue of (65) and (66), the energy density and internal pressure read

$$\begin{aligned}
\widetilde{\rho} &= \widetilde{m}_e c^2 \chi(\widetilde{y}_e)/\widetilde{\lambda}_e^3 + \widetilde{m}_p c \chi(\widetilde{y}_p)/\widetilde{\lambda}_p^3 + \widetilde{m}_n c^2 \chi(\widetilde{y}_n))/\widetilde{\lambda}_n^3, \\
\widetilde{P} &= \widetilde{m}_e c^2 \varphi(\widetilde{y}_e)/\widetilde{\lambda}_e^3 + \widetilde{m}_p c^2 \varphi(\widetilde{y}_p)/\widetilde{\lambda}_e^3 + \widetilde{m}_n c^2 \varphi(\widetilde{y}_n)/\widetilde{\lambda}_e^3.
\end{aligned} \tag{68}$$

Further simplification gives

$$\widetilde{y}_p = \left(\frac{\widetilde{a}_1 + \widetilde{a}_2 \widetilde{y}_n^2 + \widetilde{a}_3 \widetilde{y}_n^4}{1 + \widetilde{y}_n^2} \right)^{1/2}, \tag{69}$$

where

$$\begin{aligned}
\widetilde{a}_1 &= (1/4) \left[(\widetilde{Q}/\widetilde{m}_p)^2 - (\widetilde{m}_e/\widetilde{m}_p)^2 \right] \times \left[(1 + \widetilde{m}_p/\widetilde{m}_n)^2 - (\widetilde{m}_e/\widetilde{m}_n)^2 \right], \\
\widetilde{a}_2 &= (1/2) \left[(\widetilde{m}_n/\widetilde{m}_p)^2 - 1 - (\widetilde{m}_e/\widetilde{m}_p)^2 \right], \\
\widetilde{a}_3 &= (\widetilde{m}_n/2\widetilde{m}_p)^2, \quad \widetilde{Q} = \widetilde{m}_n - \widetilde{m}_p.
\end{aligned} \tag{70}$$

The ratio of proton-neutron distorted concentrations takes the form

$$\frac{\widetilde{n}_p}{\widetilde{n}_n} = \left(\frac{\widetilde{m}_p}{\widetilde{m}_p \widetilde{y}_n} \right)^3 \left[(\widetilde{a}_1 + \widetilde{a}_2 \widetilde{y}_n^2 + \widetilde{a}_3 \widetilde{y}_n^4)(1 + \widetilde{y}_n^2) \right]^{3/2}. \tag{71}$$

Appendix C   Rotating SPC

The non-spinning SPC is static and spherically symmetric. So, one needs to be clear about more general geometry which can describe rotating axisymmetric SPC. It will suffice at first to stress that the principle foundation of the spinning configurations comprises the following additional distinctive features with respect to non-spinning ones: 1) Rapid rotation causes the shape of the SPC to be flattened by centrifugal forces - flattened at poles and buldged at equator (oblate spheroid, which is second order effect in the rotation rate). 2) A rotating massive SPC drags space and time around with it. The local inertial frames are dragged by the rotation of the gravitational field, i.e. a gyroscope orbiting near the SPC will be dragged along with the rapidly rotating SPC. This is probably the most remarkable feature that could serve as a link with the general description of spacetime (also see Ter-Kazarian (2012)). Beside the geodetic procession, a spin of the body produces in addition the Lense-Thirring procession.

The axisymmetric spacetime geometry is analytically treated by Ter-Kazarian (2016a), which describes the rigorous theoretical solutions of stationary and axisymmetric rotating SPC in the framework of axisymmetric space V_4 in $3+1$ formalism. In the $3+1$ formalism, as usual, 3+1 foliations of spacetime V_4 by space-like 3-slices $\{\Sigma_t\}$ play an important role. The study of a dragging effect is assisted by incorporating with the soldering tools in order to relate local Lorentz symmetry to curved spacetime. These are the linear frames and forms in tangent fiber-bundles to the external general smooth differential manifold, whose components are so-called tetrad (vierbein) fields. Given a height-function $\widetilde{t}$, the time-like unit normal to Σ_t will be denoted by n^μ and the 3+1 decomposition of the evolution vector field by $\widetilde{t}^\mu = Nn^\mu + \beta^\mu$, where N is the lapse function and β^μ is the shift vector. The induced metric on the space-like 3-slice Σ_t is expressed as $\gamma_{\mu\nu} = g_{\mu\nu} + n_\mu n_\nu$, with D_μ the associated Levi-Civita connection and volume element ${}^3\epsilon = \sqrt{\gamma} d\widetilde{x}^1 \wedge d\widetilde{x}^2 \wedge d\widetilde{x}^3$, so that ${}^3\epsilon_{\mu\nu\rho} = n^\sigma {}^4\epsilon_{\sigma\mu\nu\rho}$. The extrinsic curvature of $(\Sigma_t, \gamma_{\mu\nu})$ in V_4 reads $K_{\mu\nu} := -(1/2)\mathcal{L}_n \gamma_{\mu\nu} = -\gamma_\mu{}^\rho \nabla_\rho n_\nu$, where $\mathcal{L}$ denotes Lie derivative. In accord, all the geometrical objects are split into corresponding components with respect to this time-slice of spacetime.

In particular, the splitting of manifold V_4 into a foliation of three-surfaces will induce a corresponding splitting of the affine connection, curvature and, thus, of the energy-momentum tensor. The 3+1 decomposition of the (matter) stress-energy tensor, measured by an adapted Eulerian observer of four-velocity n^μ in rest with respect to the foliation $\{\Sigma_t\}$, is $\widetilde{T}_{\mu\nu} = \widetilde{E} n_\mu n_\nu + \widetilde{p}_{(\mu} n_{\nu)} + \widetilde{S}_{\mu\nu}$, where the matter energy and momentum densities are given by $\widetilde{E} := \widetilde{T}_{\mu\nu} n^\mu n^\nu$ and $\widetilde{p}_\mu := -\widetilde{T}_{\nu\rho} n^\nu \gamma^\rho{}_\mu$, respectively, whereas the matter stress tensor is $\widetilde{S}_{\mu\nu} := \widetilde{T}_{\rho\sigma} \gamma^\rho{}_\mu \gamma^\sigma{}_\nu$. Latin indices running in $\{1,2,3\}$ will be employed in expressions only involving objects intrinsic to space-like Σ_t slices. That is, $\widetilde{T}^{\alpha\beta} = \widetilde{E} n^\alpha n^\beta + n^\alpha \widetilde{J}^\beta + \widetilde{J}^\alpha n^\beta + \widetilde{S}^{\alpha\beta}$. Here n^α is the unit orthogonal vector to the hypersurface Σ_t, whereas the spacetime metric g induces a first fundamental form with the spatial metric $\gamma_{\alpha\beta}$ on each Σ_t as $\gamma_{\alpha\beta} = g_{\alpha\beta} + n_\alpha n_\beta$.

The metric of the stationary and axisymmetric space V_4 in the most commonly used $3+1$ formalism includes one gauge freedom for the coordinate choice. For the spherical type coordinates $\widetilde{x}^2 = \widetilde{\theta}$ and $\widetilde{x}^3 = \widetilde{r}$,

for example, so-called quasi-isotropic gauge corresponds to $\gamma_{r\theta} = 0$ and $\gamma_{\theta\theta} = \widetilde{r}^2\gamma_{rr}$. Then, one may define the second fundamental form which associates with each vector tangent to Σ_t, and the extrinsic curvature of the hypersurface Σ_t as minus the second fundamental form. Aftermath, one can define the usual Lorentz factor $W = -n_\mu\widetilde{u}^\nu = \alpha\widetilde{u}^t$ for a fluid which is the source of the gravitational field, with conventional stress-energy tensor

$$\widetilde{T}^{\mu\nu} = (\widetilde{\rho} + \widetilde{P})\widetilde{u}^\mu\widetilde{u}^\nu + \widetilde{P}g^{\mu\nu}, \tag{72}$$

where $\widetilde{\rho}$ is the total energy density and $\widetilde{P}$ is the pressure. Hence $\widetilde{E} = W^2(\widetilde{\rho} + \widetilde{P}) - \widetilde{P}$ and $\widetilde{J}^i = (\widetilde{E} + \widetilde{P})\widetilde{v}^i$, where the fluid three-velocity $\widetilde{v}^i(i = 1, 2, 3)$ implies $\widetilde{u}^i = W(\widetilde{v}^i - \beta^i/\alpha)$. Thereby the resulting stress tensor can be written $\widetilde{S}_{ij} = (\widetilde{E} + \widetilde{P})\widetilde{v}_i\widetilde{v}_j + \widetilde{P}\gamma_{ij}$. The four-velocity for rotating fluid reads $\widetilde{u} = \widetilde{u}^i(\partial/\partial\widetilde{t}) + \Omega\partial/\partial\widetilde{\phi}$, where $\Omega = \widetilde{u}^\phi/\widetilde{u}^t$ is the fluid angular velocity as seen by an inertial observer at rest at infinity.

Consequently, the components of the energy - momentum tensor of matter with total density ρ and pressure P are given in the non-rotating anholonomic orthonormal frame as $\widetilde{T}^{(ab)} = e^a_\mu e^b_\nu\widetilde{T}^{\mu\nu}$, $\widetilde{T}^{(00)} = W^2(\widetilde{\rho} + \widetilde{P}V^2)$, $\widetilde{T}^{(11)} = W^2(\widetilde{\rho} + \widetilde{P}V^2)$, $\widetilde{T}^{(01)} = W^2(\widetilde{\rho} + \widetilde{P})V$ and $\widetilde{T}^{(22)} = \widetilde{T}^{(33)} = \widetilde{P}$, with its trace $\widetilde{T} = -\widetilde{\rho} + 3\widetilde{P}$, where V is the velocity (in units of c) with respect to the Bardeen observer $V = \varrho B(\Omega - \omega)/\alpha^2$, so $W = 1/\sqrt{1 - V^2}$.

The Petrov type D vacuum solutions associate with the gravitational field of isolated massive stationary and axisymmetric rotating SPC. They completely characterized by its mass M_{SPC} and angular momentum J_{SPC}. The two double principal null directions define "radially" ingoing and outgoing null congruences near the SPC which is the source of the field. The horizon is a 2D surface of spherical topology, where the redshift factor vanishes. The Petrov type D vacuum solutions for stationary axisymmetric rotating SPC, therefore, satisfy the Robinson's theorem for Kerr solutions in vacuum (Robinson, 1975): the solutions, (i)-are asymptotically flat, (ii)-contain a smooth convex horizon, (iii)- are nonsingular outside the horizon, and are uniquely specified by two parameters: the mass M_{SPC} and angular momentum J_{SPC}. The angular velocity of a SPC is the sum of two terms: the classical one given by the intrinsic angular velocity Ω and the frame dragging ω from the rotation of absolute space.

Near the horizon of SPC, for example, where the redshift tends to zero ($\alpha \to 0$), the angular velocity of matter Ω is completely dominated by the frame-dragging effect. Whatever the intrinsic angular momentum of the incoming matter is, this matter is forced to rotate with the local angular velocity ω, which is the maximal angular velocity at event horizon. When matter falls, say into a nonrotating black hole, it is forced to zero rotation near the horizon despite its angular momentum.

The derived global vacuum spacetime solutions describe the oblate and prolate Cauchy horizons. Whereas, an assessment of a distinction from Kerr model is given. It is shown that in the first half of its lifetime, the external physics outside of outer oblate event horizon of accretion onto the SPC with in MTBH is very closely analogous to the processes in Kerr's model. But a crucial difference between Kerr and microscopic models is the interior solutions. The interior solution of MTBH is physically meaningful, because it has smeared out a central ring singularity of the Kerr BH replacing it by the stationary axisymmetric rotating SPC inside event horizon, where the static observers exist. For brevity reasons, we have refrained from providing rigorous theoretical evolutionary paths of the equations describing the rotating black holes. The complete microscopic models of stationary and axisymmetric rotating SPCs based on the above rigorous solution will be an important topic for separate investigation elsewhere.